JOURNAL OF GEOPHYSICAL RESEARCH: PLANETS, VOL. 118, 1013–1032, doi:10.1029/2012JE004174, 2013

Mercury's hollows: Constraints on formation and composition from analysis of geological setting and spectral reflectance

David T. Blewett,[1] William M. Vaughan,[2] Zhiyong Xiao,[3,4] Nancy L. Chabot,[1] Brett W. Denevi,[1] Carolyn M. Ernst,[1] Jörn Helbert,[5] Mario D'Amore,[5] Alessandro Maturilli,[5] James W. Head,[2] and Sean C. Solomon[6,7]

Received 2 July 2012; revised 10 October 2012; accepted 26 November 2012; published 22 May 2013.

[1] Landforms unique to Mercury, hollows are shallow, flat-floored irregular depressions notable for their relatively high reflectance and characteristic color. Here we document the range of geological settings in which hollows occur. Most are associated with impact structures (simple bowl-shaped craters to multiring basins, and ranging from Kuiperian to Calorian in age). Hollows are found in the low-reflectance material global color unit and in low-reflectance blue plains, but they appear to be absent from high-reflectance red plains. Hollows may occur preferentially on equator- or hot-pole-facing slopes, implying that their formation is linked to solar heating. Evidence suggests that hollows form because of loss of volatile material. We describe hypotheses for the origin of the volatiles and for how such loss proceeds. Intense space weathering and solar heating are likely contributors to the loss of volatiles; contact heating by melts could promote the formation of hollows in some locations. Lunar Ina-type depressions differ from hollows on Mercury in a number of characteristics, so it is unclear if they represent a good analog. We also use MESSENGER multispectral images to characterize a variety of surfaces on Mercury, including hollows, within a framework defined by laboratory spectra for analog minerals and lunar samples. Data from MESSENGER's X-Ray Spectrometer indicate that the planet's surface contains up to 4% sulfur. We conclude that nanophase or microphase sulfide minerals could contribute to the low reflectance of the low-reflectance material relative to average surface material. Hollows may owe their relatively high reflectance to destruction of the darkening agent (sulfides), the presence of alteration minerals, and/or physical differences in particle size, texture, or scattering behavior.

Citation: Blewett, D. T., et al. (2013), Mercury's hollows: Constraints on formation and composition from analysis of geological setting and spectral reflectance, *J. Geophys. Res. Planets*, *118*, 1013–1032, doi:10.1029/2012JE004174.

1. Introduction

[2] Analysis of Mariner 10 color-ratio (355 to 575 nm wavelength) images of Mercury revealed that some impact craters contain patches of high-reflectance material with high ratio values [*Dzurisin*, 1977; *Schultz*, 1977; *Rava and Hapke*, 1987]. A high ratio value corresponds to a slope in the surface reflectance spectrum between ultraviolet and visible wavelengths that is shallower than that for the majority of Mercury's surface and is termed relatively "blue" in color. The three flybys of Mercury by the MErcury Surface, Space ENvironment, GEochemistry, and Ranging (MESSENGER) spacecraft, more than 30 years after the Mariner 10 encounters, returned multispectral images collected with the wide-angle camera on the Mercury Dual Imaging System (MDIS) [*Hawkins et al.*, 2007, 2009]. These data have much better radiometric calibration and a larger number of wavelengths than did the Mariner 10 images. The MESSENGER flyby data confirmed the presence of the unusual bright, bluish materials in those patches identified with Mariner 10 images, and a number of additional occurrences were noted [*Robinson et al.*, 2008; *Blewett et al.*, 2009, 2010], for example, on the floor of Sander crater and on the peak ring of the Raditladi impact basin (Figures 1 and 2).

[3] Upon MESSENGER's insertion into orbit around Mercury in March 2011, MDIS began to collect images with better spatial resolution than was possible during the flybys,

Additional supporting information may be found in the online version of this article.

[1]Planetary Exploration Group, The Johns Hopkins University Applied Physics Laboratory, Laurel, Maryland, USA.
[2]Department of Geological Sciences, Brown University, Providence, Rhode Island, USA.
[3]Lunar and Planetary Laboratory, University of Arizona, Tucson, Arizona, USA.
[4]China University of Geosciences (Wuhan), Wuhan, Hubei, China.
[5]Institute of Planetary Research, Deutsches Zentrum für Luft und Raumfahrt, Berlin, Germany.
[6]Department of Terrestrial Magnetism, Carnegie Institution of Washington, Washington, D.C., USA.
[7]Lamont-Doherty Earth Observatory, Columbia University, Palisades, New York, USA.

Corresponding author: D. T. Blewett, Planetary Exploration Group, The Johns Hopkins University Applied Physics Laboratory, Laurel, MD 20723, USA. (david.blewett@jhuapl.edu)

2169-9097/13/2012JE004174

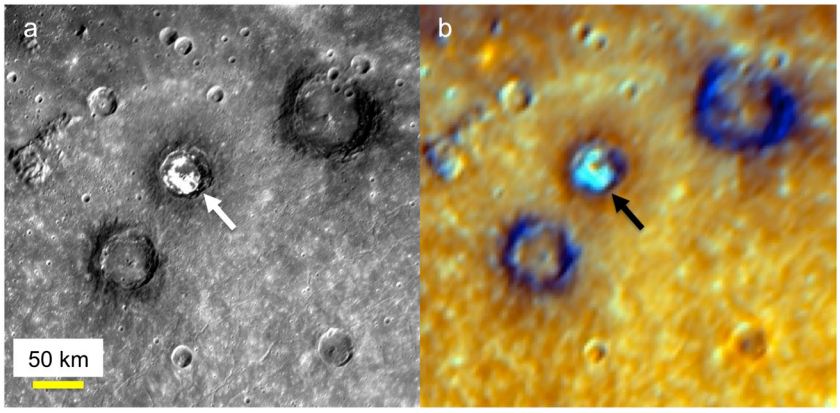

Figure 1. Images of Sander, an impact crater 47 km in diameter, obtained by MESSENGER during its first Mercury flyby. (a) Monochrome image. Deposits of unusual bright material can be seen on the crater floor. (b) Principal-component enhanced-color image [*Robinson et al*., 2008; *Denevi et al*., 2009]. The red channel is the inverse of the second principal component, which is sensitive to color variations. The green channel displays the first principal component, controlled chiefly by albedo. The blue channel is the ratio of the image at 433 nm wavelength to that at 559 nm wavelength; higher values correspond to shallower (bluer) spectral slope. Sander's floor materials (arrow) have a characteristic cyan appearance in this presentation, a result of high reflectance and relatively shallow slope. Both images are centered at 42.5°N, 154.7°E. All MDIS images in this paper have north toward the top.

including global monochrome and multispectral base maps and special high-resolution targeted observations (with pixel dimensions as small as ~12 m) obtained with the MDIS narrow-angle camera (NAC). Early in the orbital phase of the mission, high-resolution images showed that areas exhibiting high reflectance and blue color in flyby data were composed of shallow, irregular, rimless, flat-floored depressions with bright interiors and halos [*Blewett et al*., 2011]. These features were named "hollows" to distinguish them from other pit-like depressions on Mercury, including volcanic vents [*Head et al*., 2008; *Murchie et al*., 2008; *Kerber et al*., 2009, 2011] and pits that may form by collapse into a void after withdrawal of magma from a near-surface chamber [*Gillis-Davis et al*., 2009]. Hollows lacking high-reflectance interiors or halos are sometimes found adjacent to bright ones. The hollows are fresh in appearance and may be actively forming today [*Blewett et al*., 2011; *Xiao et al*., 2012]. Hollows likely form via a mechanism that involves loss of volatiles [*Blewett et al*., 2011; *Vaughan et al*., 2012], a finding at odds with several scenarios for Mercury's early history that predict a bulk composition highly depleted in volatile elements and compounds [e.g., *Boynton et al*., 2007].

[4] Completion of MESSENGER's one-Earth-year primary mission has enabled the documentation of many more examples of hollows and provided key new data on their spectral properties. All the occurrences of unusually bright, blue materials noted in low-resolution flyby images have been confirmed to consist of hollows when seen at high spatial resolution. The goals of this paper are to describe the range of geological settings in which hollows occur, to provide a global catalog of the locations of hollows and their relation to major global color units, to present data on the spectral properties of selected hollows as determined with data from MDIS, and to use the data to assess hypotheses for the mechanism(s) responsible for formation of the hollows. We suggest that hollows form in units containing a phase that is unstable when exposed to the environment at Mercury's surface. As this phase is destroyed because of high temperatures, low pressures, or intense space weathering, material is lost (e.g., by sublimation, sputtering by energetic ions, or vaporization by micrometeoroid impact), leading to the development of voids, the weakening of the residual matrix, and eventually the enlarging of the cavity to produce the visible hollows.

2. Hollows: Geological Settings

[5] Inspection of low-spatial-resolution data from MESSENGER's first Mercury flyby led initially to the association of high-reflectance, bluish material primarily with the floors of impact craters [*Robinson et al*., 2008; *Blewett et al*., 2009, 2010]. However, the subsequent flybys and especially the orbital phase of the mission revealed that in addition to floors, hollows occur in a variety of settings in and around craters as well as in locations not directly linked with impact structures. In this section we describe the types of locations in which hollows occur; these types sometimes are found in combination.

2.1. Crater Floors: Large Expanses of Hollows

[6] Several impact craters contain large expanses of high-reflectance hollows on their floors. Primary examples [*Blewett et al*., 2011] are the craters Sander (47 km diameter), Kertész [32 km, *Vaughan et al*., 2012], de Graft (68 km), and Tyagaraja (98 km), as well as the peak-cluster basin Eminescu [130 km, *Schon et al*., 2011]. In these locations large numbers of hollows have merged to produce a texture that has been described as "etched terrain" [*Blewett et al*., 2011] (Figure 3). Often the formation of the hollows appears to have been initiated around topographic highs, such as crater central peaks or the edges of crater floors at the bottom of crater walls (e.g., Warhol and the unnamed crater in Figure 4), followed by enlargement of the depressions by scarp retreat [see also *Vaughan et al*., 2012]. On the basis of the

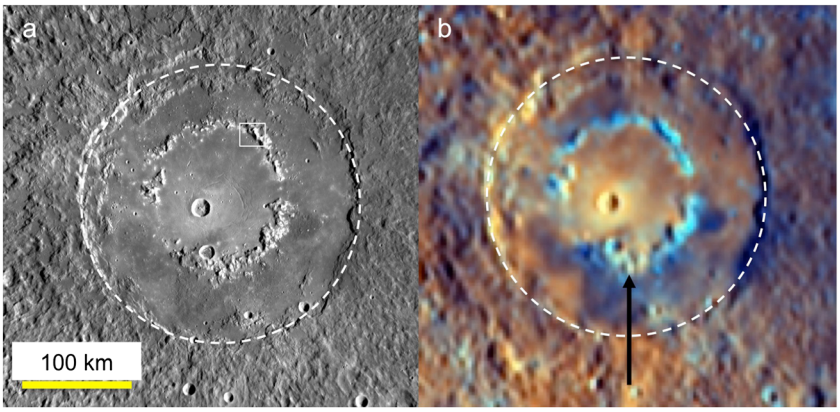

Figure 2. The Raditladi impact basin (~265 km in diameter), imaged by MESSENGER as it flew past Mercury for the first time. (a) Monochrome image. (b) Principal-component enhanced-color image. The peak-ring mountains have an unusually high reflectance and relatively blue color. The dashed line marks the main basin rim. The arrow in Figure 2b indicates the bright, blue inner peak ring. The box in Figure 2a shows the approximate location of the view in Figure 7. Color assignments in Figure 2b are the same as in Figure 1b. Images are centered at 27.1°N, 119.2°E.

morphological criteria of *Spudis and Guest* [1988], we assign Sander, Kertész, de Graft, and Tyagaraja to the Mansurian time-stratigraphic system. *Schon et al*., 2011 mapped the geology of Eminescu in detail and concluded that it is Kuiperian on the basis of the size-frequency distribution of superposed impact craters, its sharp morphology, and the presence of preserved ray segments.

2.2. Crater Floors: Smaller Areas with Hollows

[7] Less extensive fields of crater-floor hollows are found in craters such as Abu Nuwas and the unnamed crater in Figure 5. These craters are relatively old and have rims, walls, and central peaks that have been smoothed by impact erosion, suggesting they are lower Mansurian. The floors of these craters are flat and have moderate thicknesses of regolith developed on either volcanic material or impact melt.

2.3. Crater Wall Terraces and Slumps

[8] Hollows can be found on the walls of impact craters, including terraces and slump sections (Figure 6). In some cases the hollows appear along the edge of the rim or a terrace. Elsewhere hollows are found on less steeply sloped portions of the wall. The craters shown in Figure 6, located at ~50°N–60°N, have more hollows on their south-facing than their north-facing walls. This asymmetry suggests that peak solar heating may play a role in the formation of the hollows. Examples of hollows on the south-facing wall of a fresh 15 km diameter crater at 66°N were shown by *Blewett et al*. [2011, Figure 1F]. The possible role of solar heating in the formation of hollows is discussed further in section 2.9.

2.4. Central Peaks and Peak Rings

[9] Impact crater central peaks and basin peak rings [*Baker et al*., 2011] host some of the most spectacular hollows on Mercury. The Raditladi basin (~265 km in diameter) [*Strom et al*., 2008; *Prockter et al*., 2010] exhibits the albedo, color, and morphological characteristics typical of peak-ring hollows (Figures 2 and 7) [*Blewett et al*., 2011, Figure 1C]. The area of the peak ring shown in Figure 7 is distinctive for the striking flat-topped sections of the mountains and for the apron at the base. The apron may be a talus derived from mass wasting of material liberated by the hollows-forming process taking place on the top of the peak. The apron has a uniform, velvety appearance, suggesting that it is smooth at the pixel scale of the images (~16 m in Figure 7). The foot of the apron appears to be burying impact craters on the floor that are as small as 100–200 m in diameter (arrows, Figure 7). The advance of the talus over such small craters suggests that the formation of hollows on the peak ring of Raditladi is a recent and possibly ongoing event. The Raditladi basin itself does not exhibit rays but is very well preserved and is one of the younger basins on Mercury [*Strom et al*., 2008; *Prockter et al*., 2010], making it of Mansurian age.

[10] The Vivaldi basin (~200 km diameter, Calorian age) also has hollows on its peak ring (Figure 8). The peak-ring hollows of the Aksakov basin (Calorian) were discussed by *Blewett et al*. [2011]. At scales smaller than that of multiring basins, prominent hollows are located on the central peaks of the peak-cluster basin Eminescu and craters such as Kertész [*Vaughan et al*., 2012] and the craters shown in Figures 3 and 4. Two more examples of central peak hollows are presented in Figure 9.

2.5. Small Craters

[11] Two simple bowl-shaped craters that have excavated material with low reflectance (see section 2.6) are shown in Figure 10. Hollows are found on the darker areas of the continuous ejecta from these craters. Hollows have also formed on the rim and upper portion of the inner walls.

[12] Other craters in this size range appear to have a thin hollow-forming layer exposed at an approximately constant depth below the rim, extending around a large fraction of the circumference (Figure 11). This outcrop pattern implies that the lithology susceptible to development of hollows is present as a shallow stratum at these locations. The craters in Figures 10 and 11 are not rayed but have well-defined rims and hence are interpreted to be Mansurian.

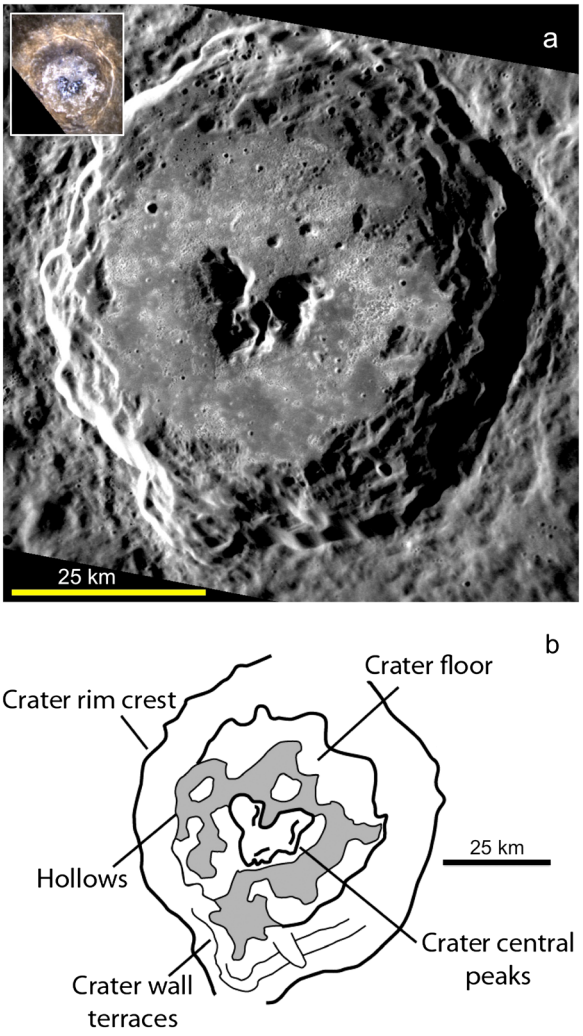

Figure 3. (a) Crater de Graft, exhibiting coalesced hollows ("etched terrain") on its floor. The crater is 68 km in diameter and centered at 22.1°N, 2.0°E. Targeted monochrome image EN0220761681M, 73 m/pixel. Inset is a red–green–blue composite of images taken through the filters at 996, 749, and 433 nm wavelength (EW0225143097I, EW0225143117G, and EW0225143101F; see also Figure 21). (b) Geologic sketch map of the major features in de Graft.

2.6. Association With Low-Reflectance Material

[13] Hollows are generally associated with material that has a reflectance lower than the global average [*Blewett et al*., 2011; *Vaughan et al*., 2012]. Low-reflectance material (LRM) is a global color unit [*Robinson et al*., 2008; *Blewett et al*., 2009; *Denevi et al*., 2009] defined by reflectance and spectral slope at visible to near-infrared wavelengths that are less than the planetary averages. Figure 10 shows two examples of hollows developed preferentially on the darker portions of the ejecta blankets of two simple craters. At two larger craters, Sher-Gil and Sholem Aleichem (Mansurian, Figure 12), hollows are seen to occur on low-reflectance areas of the walls and near-rim ejecta. The LRM in general has been suggested to have originated at depth within Mercury's crust [*Denevi et al*., 2009] on the basis of its exposure by large and small impacts. The impact process has excavated and deposited the dark material seen in Figures 10 and 12. In those cases, hollows appear to be confined to the LRM. Thus, it could be that a particular component found in the LRM is responsible for the formation of hollows because it is unstable when exposed on the surface. As discussed below in section 5 and by *Vaughan et al*. [2012], the phase that causes the LRM to have low reflectance may also be the material whose destruction/or removal leads to formation of the hollows.

2.7. Hollows and Pyroclastic Deposits

[14] Pyroclastic deposits on Mercury have high reflectance, a relatively steep ("red") spectral slope, and diffuse edges [*Kerber et al*., 2011]. Pyroclastic deposits are often associated with an irregular central depression that likely represents the vent from which the explosive volcanic products erupted. *Blewett et al*. [2011] noted hollows on the floors of Praxiteles and Tyagaraja craters that are in close proximity to reddish pyroclastic deposits and candidate vents. The collocation of bright, blue hollows and bright, red pyroclastic materials is also found in Lermontov (Mansurian, Figure 13) [*Rava and Hapke*, 1987; *Blewett et al*., 2007; *Kerber et al*., 2011] and Scarlatti craters (Calorian, Figure 14) [*Kerber et al*., 2011].

[15] Examination of hollows found in association with these pyroclastic deposits suggests that the hollows are developed in dark, bluish material. At both Lermontov and Scarlatti, it appears that the craters formed in and excavated LRM. Hollows are seen on the portions of the crater walls that are composed of LRM. The red pyroclastic deposits may be relatively thin mantles over an LRM substrate.

2.8. Small Isolated Hollows

[16] Individual hollows or small groupings that do not appear to be directly related to impacts can be found in some areas of the planet. Hollows of this kind (Figures 15a and 15b) occur on rounded knobs or flat portions of areas of rolling terrain. The examples in Figure 15 are found in units with relatively low reflectance and blue color (LRM or low-reflectance blue plains, LBP) [*Denevi et al*., 2009]. Figure 15c shows a hollow in a "dark spot" [*Xiao et al*., 2012]. Dark spots may represent a special class of low-reflectance material on Mercury distinct from LRM or LBP [*Xiao et al*., 2012].

2.9. Preference for Topographic Slopes of Maximal Heating

[17] *Blewett et al*. [2011] noted a crater at high latitude (66°N) with hollows on the equator-facing wall and rim. Such slopes would experience maximal solar heating, implying that high temperatures may be a necessary condition for development of hollows. Figure 16 presents additional examples from midlatitudes that show a tendency for hollows to form on slopes that face one of Mercury's hot poles (the two subsolar points on Mercury's equator, separated by 180° in longitude, at successive Mercury perihelia).

3. Global Distribution

[18] The global distribution of hollows found so far in MESSENGER images is shown in the map in Figure 17. The locations are tabulated in the supporting information. MESSENGER's highly eccentric orbit brings the spacecraft closest to the planet in the northern hemisphere, so the best

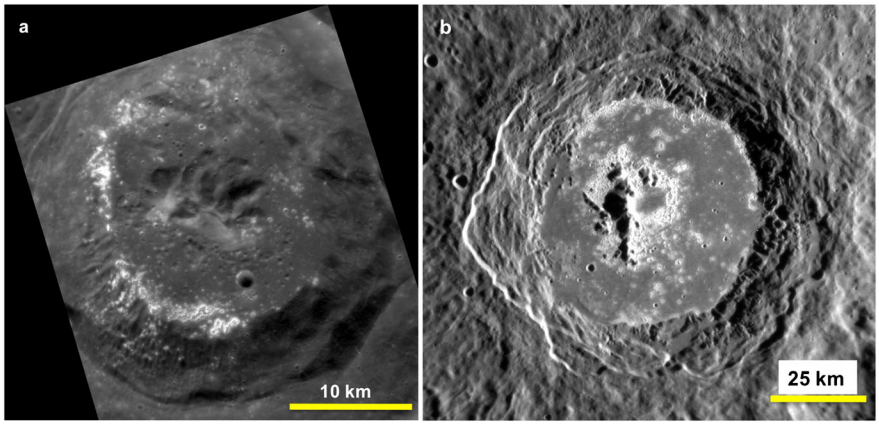

Figure 4. (a) Unnamed crater 33 km in diameter and centered at 37.8°N, 321.2°E, displaying "concentric" hollows at its floor-wall boundary. EN0241252210M, 26 m/pixel. (b) Warhol crater (2.6°S, 353.9°E, 90 km diameter). Hollows are found where smooth floor (probable impact melt) meets the wall and around the central peaks. EN0220760132M, 128 m/pixel.

spatial resolution is in the north. Because hollows are relatively small features, high spatial resolution is needed to identify them. This bias explains why the majority of identified hollows are north of Mercury's equator. Hollows are found essentially at all longitudes around the planet. Conspicuous in Figure 17 is the rarity of hollows in areas mapped as smooth plains, including the northern volcanic plains [*Head et al*., 2011]. Smooth plains are essentially all Calorian in age [*Spudis and Guest*, 1988; *Denevi et al*., 2012].

[19] The occurrence of hollows in low-reflectance units noted above in the discussion of specific examples (e.g.,

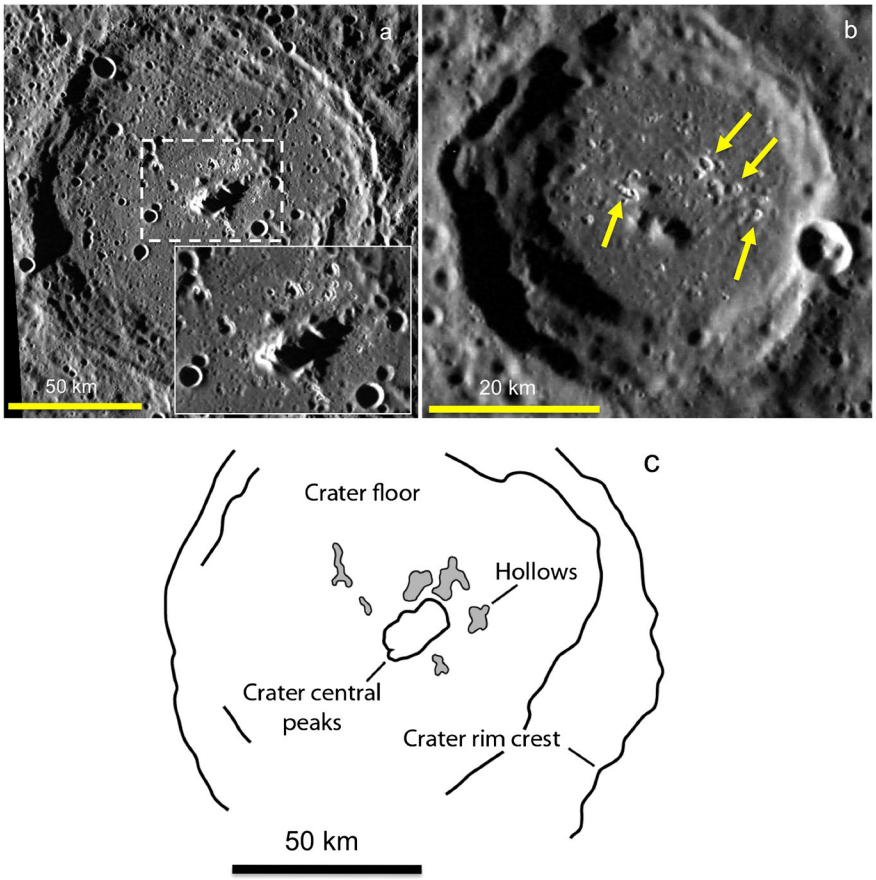

Figure 5. Hollows on floors of partially degraded craters. (a) Small hollows north of the central peak of Abu Nuwas, 117 km in diameter and centered at 17.6°N, 338.8°E. EW0212808886G, 160 m/pixel. (b) Unnamed crater 45 km in diameter and centered at 14.4°N, 333.2°E. EW0212939298G, 166 m/pixel. (c) Geologic sketch map of Abu Nuwas.

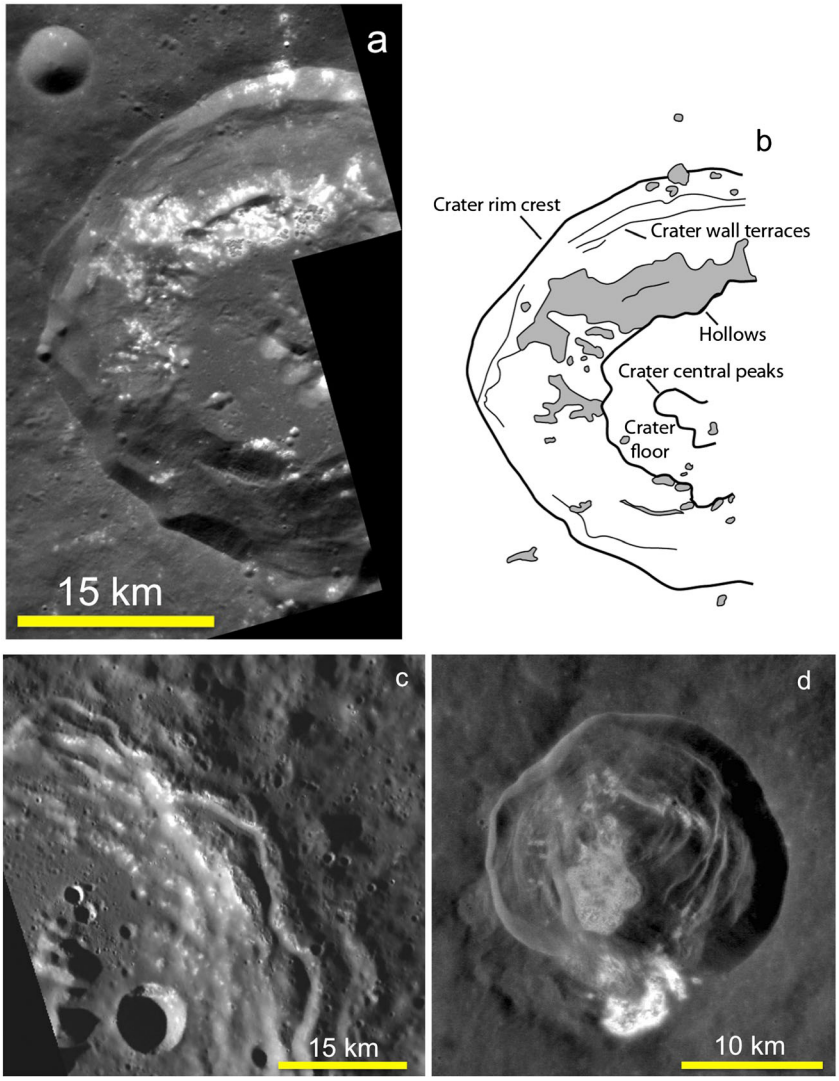

Figure 6. Hollows on impact crater wall terraces and slumps. (a) A crater 35 km in diameter. Mosaic of targeted NAC images EN0226033164M and EN0226033173M, centered at 50.8°N, 319.9°E, 27 m/pixel. (b) Geologic sketch map of image in Figure 6a. (c) Wall of crater 72 km in diameter. EW0213069011G, image centered at 60.1°N, 320.8°E, 125 m/pixel. The craters in Figures 6a and 6c lack rays but have well-preserved morphology, indicative of Mansurian age. (d) The rayed crater Dominici (Kuiperian, 20 km diameter), centered at 1.26°N, 323.5°E. Targeted NAC image EN0253965560M, 50 m/pixel. Other prominent Kuiperian craters hosting hollows include Ailey, Balanchine, Basho, Cunningham, and Degas.

Figures 10, 12–15) is confirmed in the global map, especially in the longitude range ~280°E to 330°E, which is dominated by LRM. Minor examples of hollows occur in LBP, e.g., Figure 15a. The hollows found within expanses of high-reflectance red plains (HRP) [*Robinson et al*., 2008; *Denevi et al*., 2009], such as the interior of the Caloris basin, have formed in LRM that was excavated from beneath the HRP by later impacts (e.g., Sander crater, Figure 1) [e.g., *Ernst et al*., 2010].

4. Formation Hypotheses

[20] A number of processes can produce rimless, irregular depressions on planetary surfaces, including secondary cratering and volcanism. Hollows have flat floors and irregular outlines, as opposed to the cone or bowl shapes typical of primary impact craters, the herringbone pattern of secondary clusters or chains [e.g., *Oberbeck and Morrison*, 1973], or the circular but shallower morphology of distant secondary craters [*Xiao and Strom*, 2012].

[21] *Blewett et al*. [2011] discussed key differences that distinguish hollows from volcanic depressions (e.g., vents formed by explosive eruptions [*Kerber et al*., 2011], or pit craters resulting from caldera-like collapse following withdrawal of magma from a near-surface chamber [*Gillis-Davis et al*., 2009]). Major characteristics related to morphology, geologic setting, and color separate hollows from depressions on Mercury that are recognized to be of volcanic origin.

[22] The Moon's Ina structure [*Whitaker*, 1972; *El Baz and Worden*, 1972; *El-Baz*, 1973; *Schultz*, 1976; *Strain and El Baz*, 1980], sometimes called the "D caldera," is an enigmatic, shallow depression ~2 km wide, in Lacus Felicitatis

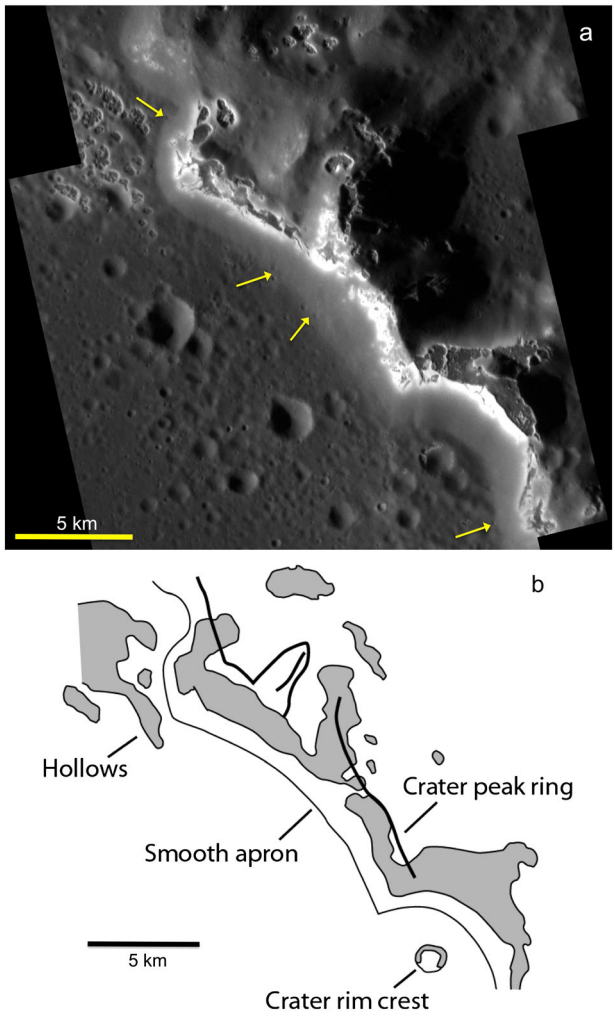

Figure 7. (a) Hollows on the floor and peak ring of Raditladi basin. A box in Figure 2 indicates the location of this image. Note the smooth apron at the base of the peak mountain, possibly formed by downslope movement of material released by the hollows-forming process taking place above. Arrows indicate small craters on the floor that appear to be partially buried by the edge of the apron. Mosaic of targeted NAC images EN0221023165M and EN0221023170M, 16 m/pixel; this view is centered at ~28.5°N, 120.0°E. (b) Geologic sketch map of the scene in Figure 7a.

that bears a superficial resemblance to Mercurian hollows. Ina, the best-known example of a class of similar mare features, consists of a bulbous, smooth elevated unit surrounded by a rougher lower unit. Portions of the lower unit appear bright in high-Sun images. Ina's location on a broad, low-relief topographic rise led to the conjecture that its formation involved volcanic activity such as a caldera-like collapse, the extrusion of magma with unusual composition or texture, and perhaps the deposition of sublimates. Studies of Ina's color trends and crater populations led *Schultz et al*. [2006] to conclude that Ina is very young, and they suggested that explosive outgassing events could maintain the optical immaturity of the regolith. *Robinson et al*. [2010] examined Ina with high-resolution images from the Lunar Reconnaissance Orbiter Camera Narrow Angle Camera (LROC-NAC). The LROC-NAC crater size-frequency data extend to smaller diameters than prior counts and show that the Ina smooth unit is probably the same age as the surrounding mare material. The lower unit is more lightly cratered but is unlikely to be as young as the data of *Schultz et al*. [2006] indicated. The LROC-NAC images reveal that the bright patches of Ina's lower unit are associated with steep slopes and a high abundance of blocks and boulders, which would explain the high reflectance and immature color properties found by *Schultz et al*. [2006]. The floor materials are similar to relatively unweathered high-titanium basalts [*Staid et al*., 2011]. In addition, *Robinson et al*. [2010] found no evidence for the presence of bright condensates.

[23] A number of characteristics distinguish hollows on Mercury from Ina. Importantly, hollows are found in a range of geologic and topographic settings (basin and crater central peaks, crater floors, walls, rims and ejecta, and plains; see section 2) whereas Ina-like features appear to be restricted to flat areas of the maria [*Stooke*, 2012]. Their distribution implies that hollows form by a process related to the nature of the material exposed at these locations, whereas Ina may be a result of special local conditions of mare basalt emplacement [e.g., inflated flows, *Garry et al*., 2012]. The sizes of the two types of features also contrast greatly. Expanses of hollows such as those in Tyagaraja and Sander [*Blewett et al*., 2011] can be several tens of kilometers across, but Ina (the largest of its kind) is less than 3 km in its long dimension. In terms of color, Ina resembles nearby immature mare crater materials [*Staid et al*., 2011], whereas hollows have bluer spectra than fresh craters on Mercury [*Robinson et al*., 2008; *Blewett et al*., 2009, 2011] (see also section 5). These color characteristics indicate that a compositional contrast exists between the hollows and the surrounding terrain but not between Ina and its neighboring mare. Ina may have originated through some type of collapse process, but further work is needed to determine whether study of lunar Ina-type features can help in the understanding of Mercurian hollows.

[24] Several lines of evidence point to an origin of the hollows that involves loss of volatiles. These include (a) the relatively high abundances of sulfur, sodium, and potassium in Mercury's surface as determined by MESSENGER elemental remote sensing [*Nittler et al*., 2011; *Peplowski et al*., 2011, 2012; *Evans et al*., 2012; *Weider et al*., 2012]; (b) the resemblance of hollows to the "Swiss-cheese" terrain found on the south polar cap of Mars (cf. supporting information of *Blewett et al*. [2011]) that consists of rounded, irregular, rimless depressions formed by sublimation of CO_2 ice [*Malin et al*., 2001; *Byrne and Ingersoll*, 2003]; and (c) the tendency for hollows to form on equator- or hot-pole-facing slopes (section 2.9), suggesting that peak solar heating could contribute to their formation.

[25] In the two subsections below, we examine two hypotheses for the origin of hollows that involve loss of volatiles. For each hypothesis, there are two questions to be addressed: (a) the source of the volatiles, and (b) the mechanism by which volatiles are lost and depressions are initiated and enlarged. These hypotheses are not mutually exclusive, and it could be that both formation mechanisms are operating on Mercury to form hollows in different geologic contexts. At present, there is not sufficient evidence to discriminate between these hypotheses.

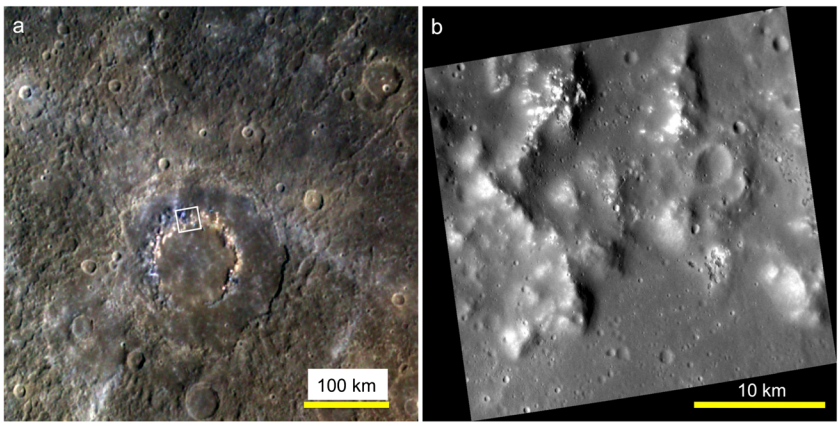

Figure 8. Hollows on the peak ring of Vivaldi basin. (a) Color-composite image illustrates the high reflectance and color associated with hollows. The view is centered at 15.0°N, 274.7°E. Color composite of images at 996, 749, and 433 nm wavelength (EW0211415166I, EW0211415174G, EW0211415168F), 1.2 km/pixel. Box shows approximate location of the high-resolution view in Figure 8b. (b) Targeted NAC image (EN0229192231M) for a portion of the Vivaldi peak ring; image center at 14.6°N, 273.8°E, 25 m/pixel.

4.1. Sequestered Volcanic Volatiles

[26] *Blewett et al*. [2011] described a candidate hollow-forming process in which magmatic volatiles play a leading role. It is clear that voluminous extrusive and explosive volcanism took place on Mercury and that volcanic units cover much of the planet [*Robinson and Lucey*, 1997; *Head et al*., 2008, 2009, 2011; *Denevi et al*., 2009]. Mercury's slow rotation and lack of an atmosphere produce nights that are long and cold. Therefore, quantities of magmatic gases and fumarolic minerals from eruptions could condense on the low-temperature nightside surface and along fractures within the subsurface (Figure 18, step 1) and could be buried by ongoing volcanic activity (e.g., emplacement of extensive thicknesses of pyroclastic deposits or lava flows). The localized volatile-rich deposits would thus be sequestered beneath cap rock (Figure 18, step 2) until exposed and redistributed by impact cratering (Figure 18, step 3). As volatiles sublime from the crater interior and ejecta, depressions form and enlarge by collapse and mass wasting, producing hollows. In the case of volatiles liberated from beneath cap rock, it is possible that highly volatile species are involved.

[27] In the buried volcanic volatiles hypothesis, materials hosting hollows might have been altered through contact with the volatiles. Such phases could be responsible for the high reflectance and characteristic color of the hollows [cf., *Dzurisin*, 1977]. Gradual desiccation or another form of destruction of the altered minerals in the harsh surface environment could account for the transition from hollows with bright interiors and halos to those without. If the volatile-sequestration concept applies to Mercury, the lack of hollows found in areas of high-reflectance plains (Figure 17) may indicate that those volcanic materials were lower in volatile content than the deposits that comprise low-reflectance materials.

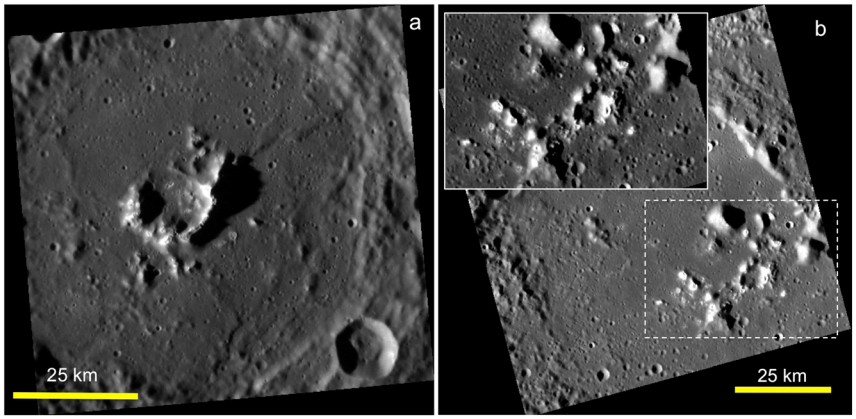

Figure 9. Hollows on the central peaks of two Mansurian craters. (a) Mickiewicz crater (102 km diameter, 23.1°N, 257.0°E). Image EN0216587102M, 145 m/pixel. (b) Velázquez crater (128 km diameter, 37.8°N, 304.2°E). Image EW0213416991G, 162 m/pixel. Inset shows a closer view of the area in the dashed box.

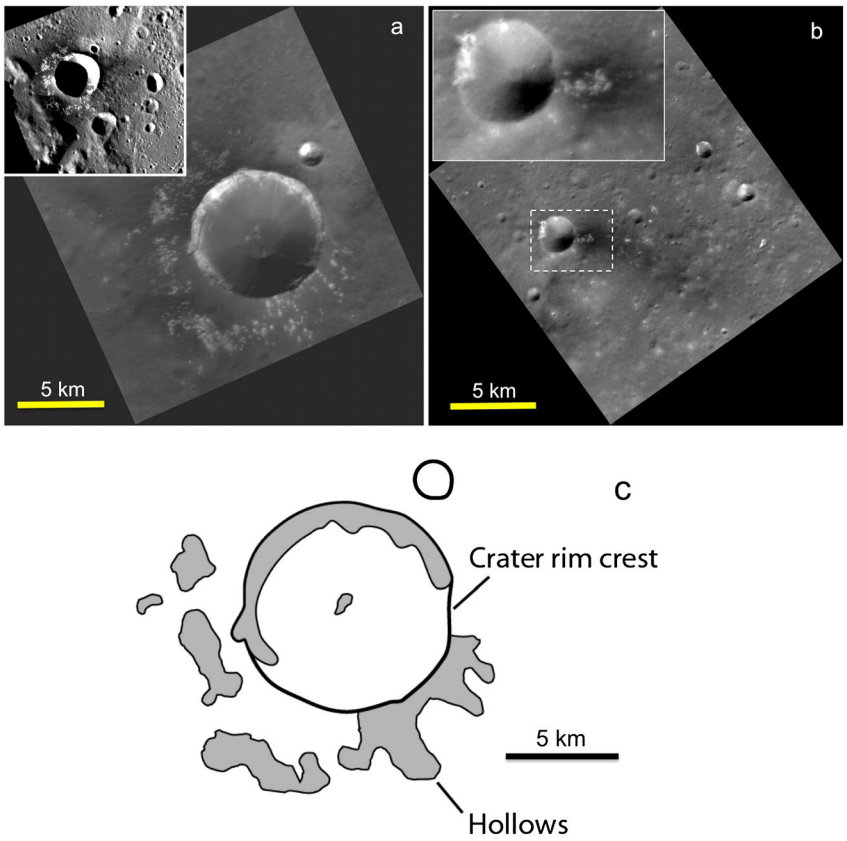

Figure 10. Hollows on rims and ejecta of simple bowl-shaped craters. Both have LRM ejecta. (a) Crater 9 km in diameter in image EN0233815896M (57.2°N, 125.8°E, 21 m/pixel). Inset shows the low reflectance of the portions of the ejecta on which the hollows are found (EW0220893170G, 60 m/pixel). (b) Small (3.5 km diameter) crater with hollows on the rim and on low-reflectance ejecta that extends east of the rim. Image EN0233900643M, 55.1°N, 113.3°E, 26 m/pixel. (c) Geologic sketch map of the crater in Figure 10a.

[28] Chlorine is a volatile element associated with terrestrial volcanic gases. Chlorine-bearing compounds could be precipitated as fumerolic minerals or created as alteration products in the buried volatiles scenario. Chlorine has a large neutron capture cross-section and emits relatively strong gamma rays, but it has not been clearly detected in the analysis of MESSENGER Gamma-Ray Spectrometer data [*Evans et al*., 2012]. MESSENGER X-Ray Spectrometer data indicate an upper limit of 0.2 wt % Cl over broad regions of the surface [*Nittler et al*., 2011]. Of course, the low spatial resolution (several hundred kilometers at best) of the orbital gamma-ray and X-ray data might prevent detection of a chlorine signal from even the largest exposures of hollows.

4.2. Volatile-Bearing Lithology

[29] The buried volatiles scenario outlined above posits "bulk" accumulations of volatiles that are lost upon exposure at or near the surface. In this section, we discuss the formation of hollows by loss of volatile-bearing phases that are instead an inherent component of upper crustal material.

[30] Prior to the return in 2011 of high-spatial-resolution images from MESSENGER's orbital phase that revealed the detailed morphology of the hollows, unusual bright, blue materials associated with impact structures were known as "bright crater-floor deposits". *Blewett et al*. [2009] mentioned the possibility that lobate bright crater-floor deposits such as those on the floors of the craters Sander and Kertész could be a result of special lithologies produced by differentiation of impact melts. Particularly given the extremely high velocities of impactors that strike Mercury (as great as 80 km/s) [*Marchi et al*., 2005; *Le Feuvre and Wieczorek*, 2008, 2011], certain impacts might produce large quantities of melt that could form deep ponds and undergo differentiation.

[31] *Vaughan et al*. [2012] presented a detailed model for the formation of hollows that involves differentiation of impact melt. Their scenario accounts for the abundance of sulfur detected at the Mercurian surface [*Nittler et al*., 2011; *Weider et al*., 2012], and they concluded that the flotation of a layer rich in sulfide minerals would take place in an impact melt of the magnesian, komatiite-like material similar to compositions inferred from MESSENGER X-Ray Spectrometer measurements [*Nittler et al*., 2011; *Weider et al*., 2012].

[32] Another means of producing concentrations of sulfide minerals was described by *Helbert et al*. [2012], who noted that Mg-rich komatiitic magmas would tend to bind sulfur from sulfur-rich materials encountered as the melts rise within Mercury's crust. The resulting MgS, CaS, or MnS would float on erupted lavas as a slag-like accumulation.

[33] Rather than, or in addition to, a melt-related process producing a sulfide-rich layer in which a volatile-bearing phase is concentrated, it is also possible that a volatile-bearing and hollow-forming phase is distributed throughout

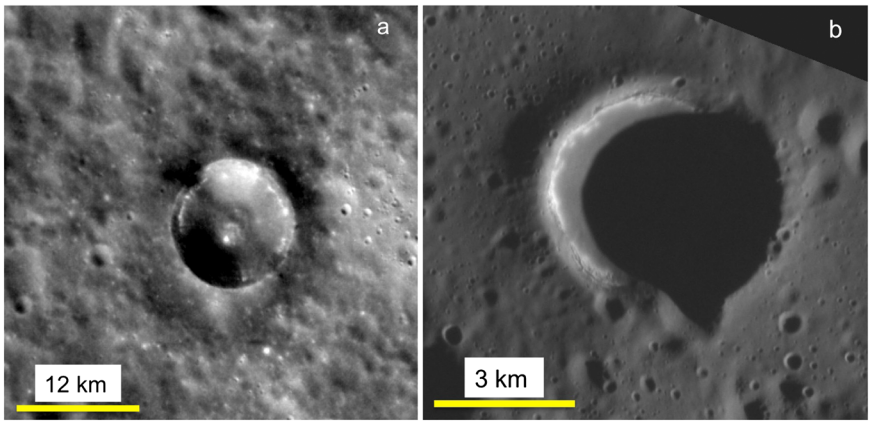

Figure 11. Examples of a high-reflectance layer exposed on the upper wall of a small crater, suggesting that hollow-forming material is present as a stratum in the near subsurface. (a) Portion of image EN0209938157M, centered near 27.9°N, 19.9°E, 111 m/pixel. (b) Targeted NAC image EN0231351516M, 57.3°N, 115.0°E, 14 m/pixel.

certain rock types. Contact heating of such rocks by impact melt, lavas, or intrusions could account for the tendency for hollows to form around crater floor perimeters and the base of central peak mountains (Figure 19, cf. Figure 4). In addition, there are hints that sulfides may be slightly unstable when exposed to Mercury daytime temperatures [*Helbert et al*., 2012; *Vaughan et al*., 2012]. As discussed in section 2.9, there is evidence that formation of hollows is favored on surfaces that experience the greatest solar heating. Thus, high surface temperatures may be a condition necessary for, or at least conducive to, hollow formation.

[34] Sputtering by energetic ions and/or micrometeoroid impact melting and vaporization are other processes that could contribute to the destruction of volatile-bearing phases (Figure 20). A depletion of sulfur on the surface of asteroid Eros relative to the element's abundance in ordinary chondrites was discovered by the Near Earth Asteroid Rendezvous X-ray spectrometer [*Trombka et al*., 2000; *Nittler et al*., 2001]. Troilite (FeS), the major sulfur-bearing mineral in ordinary chondrites, is vaporized more easily than silicates [*Killen*, 2003; *Kracher and Sears*, 2005]. Experiments that simulated micrometeoroid impact vaporization (via laser pulse heating) and solar-wind irradiation demonstrated that a two-stage process of vaporization of FeS followed by ion bombardment leads to loss of sulfur [*Loeffler et al*., 2008]. Calcium and magnesium sulfides may be susceptible to a similar destruction process.

[35] The processes hypothesized to destroy sulfides on Eros are much more vigorous on Mercury. Mean micrometeoroid impact velocities are much greater at Mercury (~20 km/s) [*Cintala*, 1992] than at the location of Eros (~9 km/s) [*Killen*, 2003]. The flux of micrometeoroids is also greater at Mercury. Even during quiet magnetospheric conditions, solar wind ions gain access to much of Mercury's surface [*Sarantos et al*., 2007]. This access is enhanced by magnetospheric substorms (magnetotail "loading and unloading" events), which can lead to the entire dayside surface of the planet being exposed to the solar wind for brief periods, followed by the precipitation of energetic ions onto the nightside of the planet [*Slavin et al*., 2010]. Because of Mercury's high surface gravitational acceleration, ejected sulfur will not easily escape the surface as it does on Eros.

[36] Sulfur in Mercury's surface is correlated with the abundances of calcium and magnesium [*Nittler et al*., 2011; *Weider et al*., 2012]. *Weider et al*. [2012] have shown that older, intercrater units and heavily cratered terrains have higher sulfur contents than do the northern smooth plains and the Caloris interior plains. The distribution of hollows (Figure 17) indicates that hollows are absent from the northern smooth plains and Caloris interior plains. The northern smooth plains and Caloris interior plains have a higher reflectance and are redder than the global average. These observations support the idea that regional variations in sulfide mineral abundance play an important role in controlling the spectral character of the surface and in the formation of hollows.

[37] Other than sulfur, the volatile elements sodium (Na) and potassium (K) have been measured on Mercury's surface through analysis of data from the MESSENGER Gamma-Ray Spectrometer [*Evans et al*., 2012; *Peplowski et al*., 2011, 2012]. The relatively high global average sodium abundance (2.9 wt %) [*Evans et al*., 2012] and petrological modeling of crystalizing melts of candidate Mercury compositions [*Stockstill-Cahill et al*., 2012] suggest that Na-rich plagioclase (albite) could be present. Sodium is a constituent of Mercury's exosphere [*Potter and Morgan*, 1985], and the exospheric species originates from the planetary surface. Sodium is supplied to the exosphere by such processes as thermal evaporation and space weathering (micrometeoroid vaporization, sputtering, and photon-stimulated desorption) [*Domingue et al*., 2007]. Therefore, the destruction of a sodium-bearing phase could be involved in the formation of hollows. At present, only the global average surface sodium abundance has been derived [*Evans et al*., 2012]. If spatially resolved measurements for specific geologic units (e.g., plains, LRM) can be performed as the mission progresses, then the relationship between sodium abundance and units hosting hollows can be better assessed.

[38] Potassium is another volatile element found in both the surface [*Peplowski et al*., 2011, 2012] and exosphere [*Potter and Morgan*, 1986]. Potassium is supplied to the exosphere by the same processes as described above for sodium. As noted by *Weider et al*. [2012], the low abundance of potassium generally (2000 ppm in the northern plains and

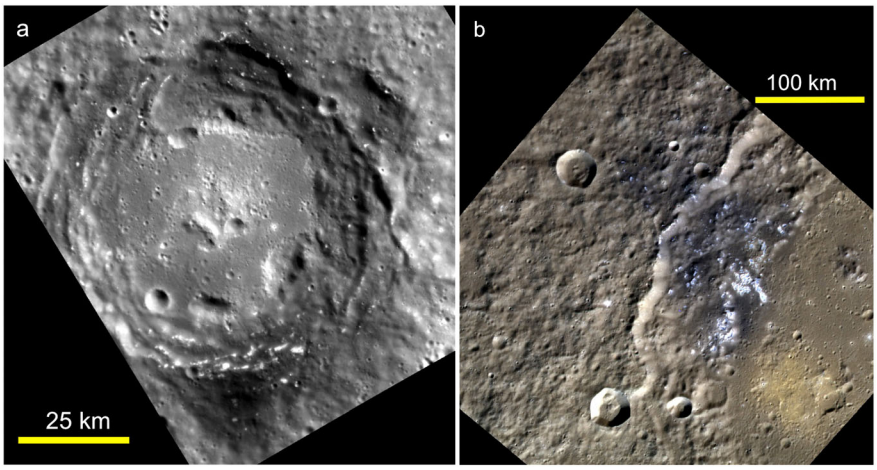

Figure 12. The association of hollows with the LRM color-compositional unit. (a) Hollows on the dark portions of the walls and ejecta of Sher-Gil crater (76 km diameter). Image EN0231267850M, centered at 45.1°S, 135.3°E, 102 m/pixel. (b) LRM and hollows on western rim of Sholem Aleichem crater (196 km diameter). Color composite at wavelengths of 996, 749, and 433 nm, respectively as red, green, and blue (RGB). Images EW0241962499I, EW0241962491G, and EW0241962495F, centered at 50.1°N, 266.4°E, 148 m/pixel.

~500 ppm in the surroundings) is too low for K-rich feldspar to be a major rock-forming mineral. The relatively large volumes of material lost during hollow formation [*Vaughan et al*., 2012] suggest that more abundant volatile elements (e.g., sulfur, with 2.3 wt % abundance in intercrater plains and heavily cratered terrain [*Weider et al*., 2012] or sodium, with 2.9 wt % global average [*Evans et al*., 2012]) are more likely to be involved in hollow formation than is potassium.

[39] Whatever the identity of the volatile element or phase, the formation of a hollow by solar heating, ion sputtering, and/or micrometeoroid melting and vaporization is initiated at a particular location because of local variations in the abundance of the phase susceptible to loss, or otherwise favorable physical conditions (Figure 20, panels 1 to 3). Hollows often have flat floors and appear to have approximately constant depths of several tens of meters [*Blewett et al*., 2011; *Vaughan et al*., 2012]. The ultimate depth of hollows could be controlled either by the thickness of the layer containing the volatile-bearing phase, or by development of a thermally insulating and mechanically resistant lag that prevents further loss of volatiles. These two scenarios are depicted in Figure 20, panel 4.

5. Spectral Reflectance Case Study

[40] Studied from Earth-based telescopes, Mercury's reflectance spectrum in the wavelength range from visible to near-infrared (~400 to 1000 nm) exhibits no strong absorption features [e.g., *McCord and Clark*, 1979; *Vilas*, 1988; *Warell*, 2003; *Warell and Blewett*, 2004; *Warell et al*.,

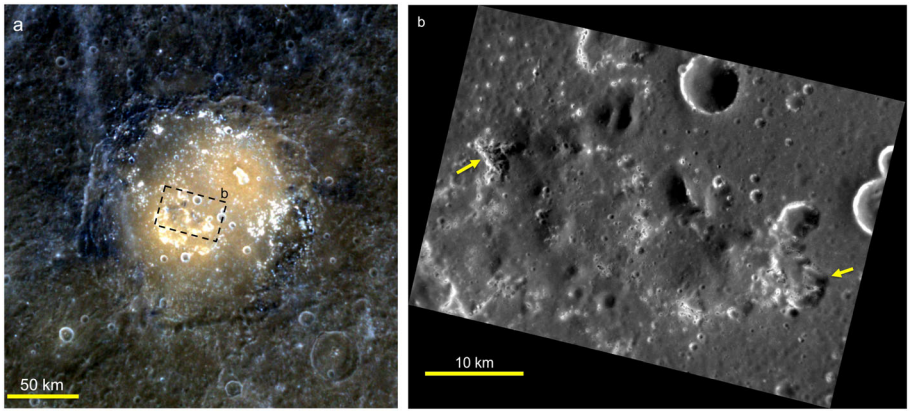

Figure 13. Hollows and pyroclastic material on the floor of Lermontov crater (166 km diameter, 15.3°N, 311.1°E). (a) Color composite at wavelengths of 996, 749, and 433 nm as RGB. Images EW0211111577I, EW0211111597G, and EW0211111581F, 451 m/pixel. Dashed box approximates the area shown in Figure 13b. The bright reddish material on the crater floor was likely produced in pyroclastic eruptions. The dark blue material forming much of Lermontov's walls and the area to the north is LRM. (b) Targeted NAC image for an area of Lermontov's floor, EN0223702050M, 30 m/pixel. Hollows are scattered across Lermontov's floor and walls and occur on the rims of small impact craters and the walls of irregular rimless depressions (arrows) that may be volcanic vents.

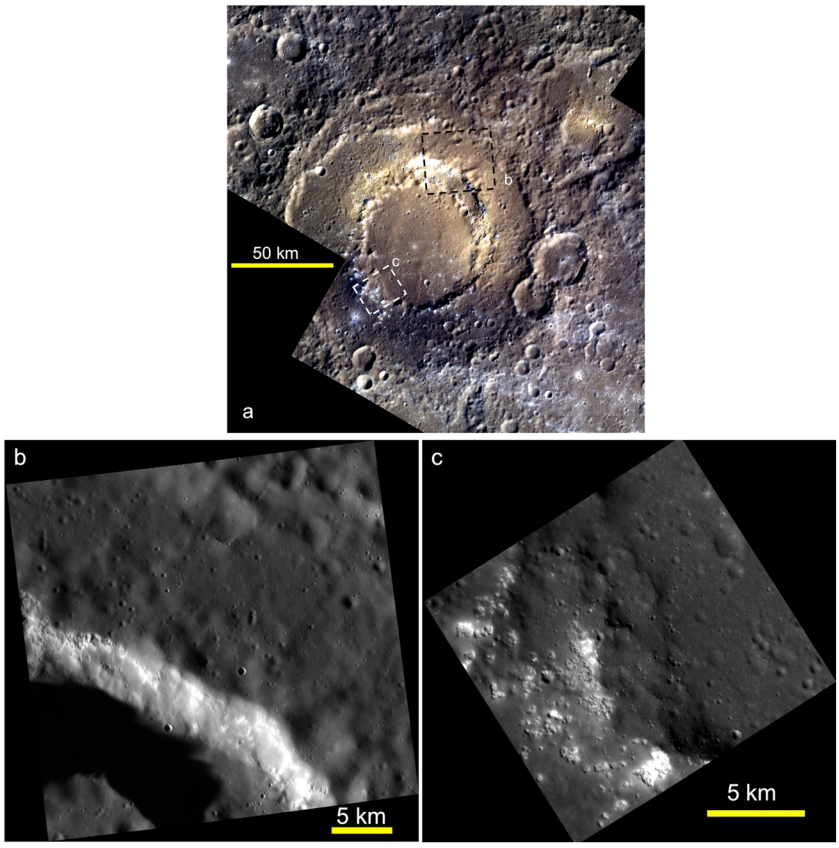

Figure 14. Hollows and pyroclastic material within Scarlatti crater (132 km diameter, 40.8°N, 258.8°E). (a) Color composite mosaic at wavelengths of 996, 749, and 433 nm as RGB. Images EW0242045882I, EW0242004051I, EW0242045874G, EW0242004043G, EW0242045878F, EW0242004047F, 202 m/pixel. Dashed boxes indicate the areas of high-resolution images in Figures 14b and 14c. Reddish pyroclastic material has mantled much of the northern half of the crater. A large, elongated, vent-like depression has replaced the northern portion of the peak ring. Hollows are found within dark, blue material that forms Scarlatti's peak ring and the area between the peak ring and the southern rim. LRM is also found to the north and east of Scarlatti. (b) High-resolution targeted NAC view of a section of the large vent seen in Figure 14a. Image EN0231821310M, 29 m/pixel. Hollows are developed in the rim and walls of the vent. (c) Hollows on the southern peak ring. Targeted NAC image EN0244488176M, 14 m/pixel.

2006]. This result was confirmed during the MESSENGER flybys with spatially resolved spectra obtained with the multispectral camera (MDIS) [*Robinson et al*., 2008] and the Mercury Atmospheric and Surface Composition Spectrometer (MASCS) [McClintock *et al*., 2008]. The planet's major terrains differ principally in albedo and overall spectral slope [*Robinson et al*., 2008; *McClintock et al*., 2008; *Denevi et al*., 2009].

[41] Observations from orbit afford the opportunity to characterize the spectral reflectance of the surface at higher spatial resolution and with more favorable viewing and illumination conditions than was possible during the flybys. Figure 21 is a color-composite view of the area of de Graft crater obtained as a set of special targeted color observations. This set employed eight of the MDIS narrow-band color filters, with central wavelengths at 433, 480, 559, 629, 749, 828, 899, and 996 nm. The pixel dimension of these images is more than an order of magnitude smaller than that of the global flyby image cube analyzed by *Blewett et al*. [2009] (434 m/pixel versus 5 km/pixel). Images were processed through the standard MDIS calibration sequence in the U.S. Geological Survey's Integrated Software for Imagers and Spectrometers and were map projected. A photometric normalization [*Domingue et al*., 2011] was applied to convert the image values to reflectance at standard geometry (incidence and phase angles of 30°, and emergence angle of 0°). Although *Domingue et al*. [2011] noted difficulties in photometric correction of images obtained at extreme geometries (phase angles >110° and incidence or emergence angles >70°), the de Graft image used here was collected under conditions that are well within the range for which the correction is successful: phase = 39.3°, incidence = 26.8°, emergence = 22.5°. Difficulties in mosaicking due to variations in scattered light [*Domingue et al*., 2011] are avoided by restricting the present study to a single MDIS image cube. The MASCS instrument includes a spot spectrometer, the Visible and InfraRed Spectrograph (VIRS), that is conducting global mapping of Mercury's surface at high spectral resolution in the wavelength range ~300–1400 nm [*McClintock et al*., 2008]. However, VIRS footprints are generally larger than many of the small surface features that are of interest here; in addition, the radiometric calibration and photometric

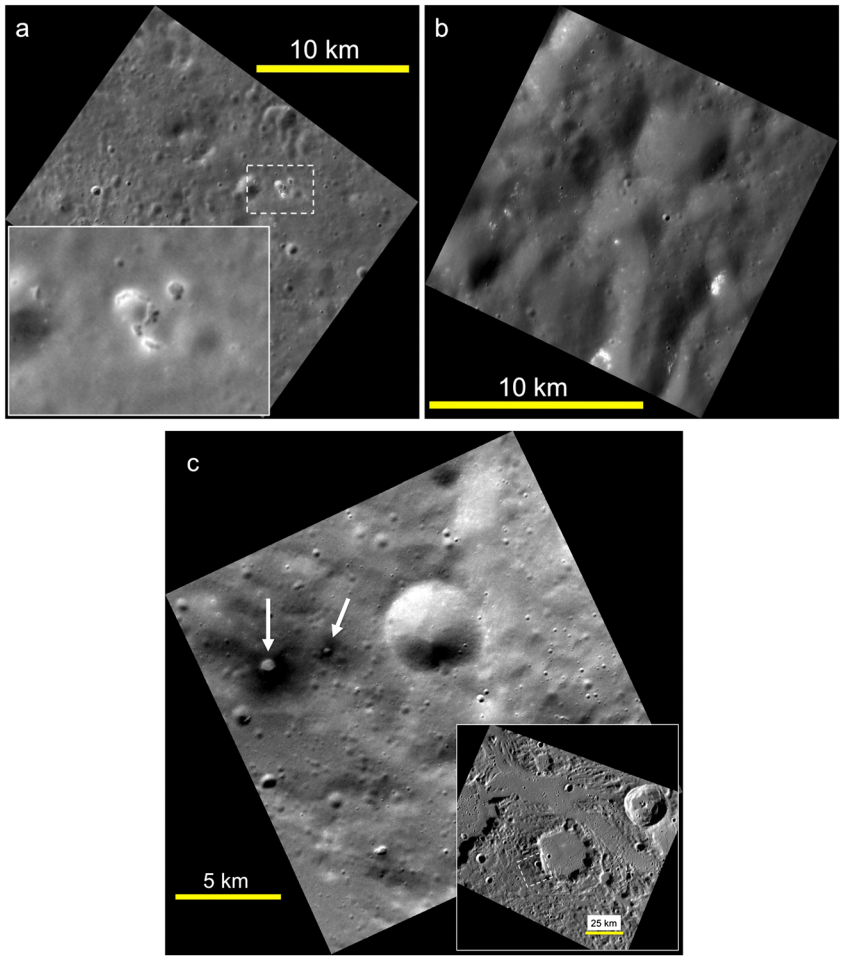

Figure 15. Isolated hollows. (a) Small cluster near 44.6°N, 135.4°E. Targeted NAC image EN0215894086M, 16 m/pixel. Inset is a zoom on the area in the dashed box. This area is in low-reflectance blue plains (LBP) [*Denevi et al*., 2009]. (b) Small hollows near 40.6°N, 305.9°E. Image EN0238696735M, 15 m/pixel. (c) Hollows in a "dark spot" (arrows) [*Xiao et al*., 2012]. Dashed box in inset shows location of main image. Main image is targeted NAC EN0234070626M, 17 m/pixel, centered at 59.8°N, 116.1°E. Inset is EW0216154618G, 217 m/pixel.

correction for the complicated VIRS data set are not yet as far advanced as those for MDIS. Therefore, we use only MDIS data for the current analysis.

[42] Reflectance spectra for a number of areas of interest (Figure 21) are presented in Figure 22a. Figure 22b shows the spectra divided by the spectrum of the intermediate terrain (IT), a widespread spectral unit on Mercury [*Denevi et al*., 2009], emphasizing the differences in albedo and slope among the different types of material in this area.

[43] The spectra in and around de Graft include most of the major and minor color types recognized in the flyby data: IT, LRM, reddish units, fresh ray material, and hollows [*Robinson et al*., 2008; *Blewett et al*., 2009; *Denevi et al*., 2009]. The hollows are nearly twice as reflective at 749 nm as is Mercury on average (represented in Figure 22 by the IT). All Mercury surfaces have reflectances that increase toward longer wavelengths. The relative reflectance plot (Figure 22b) illustrates that the spectra of hollows are much less steeply sloped than other types of material, resulting in the negative slope of relative reflectance spectra for the hollows.

[44] The lack of strong absorption bands at visible to near-infrared wavelengths makes identification of the composition of the major phases in Mercury's regolith difficult. Figure 23 shows the de Graft spectra of Figure 22a plotted together with laboratory spectra for a variety of potential analog materials. The strikingly low albedo of Mercury is apparent when MDIS spectra are plotted on the same scale as the analogs. For example, the IT and LRM have about the same reflectance as ilmenite. The hollows, which are among the brightest materials on the planet, have lower reflectance than a mature Apollo 16 highland soil. The low reflectance of Mercury has been noted previously [*Denevi and Robinson*, 2008; *Denevi et al*., 2009; *Warell et al*., 2010; *Lucey and Riner*, 2011; *Riner and Lucey*, 2012].

[45] Because overall reflectance and spectral slope are the chief distinguishing factors of Mercury's surface in the MDIS wavelength range, we can conveniently condense the major spectral variations into two parameters: reflectance at 749 nm and the ratio of reflectance at 433 nm to that at 749 nm. Figure 24 is a ratio-reflectance plot for the Mercury

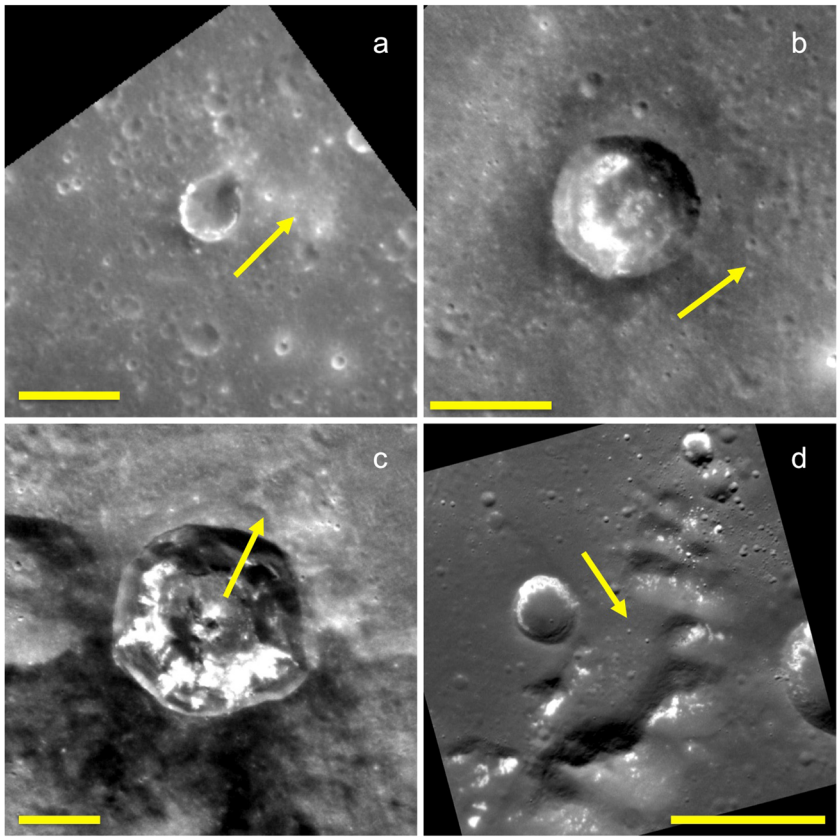

Figure 16. Hollows on slopes that experience maximal solar heating. The arrows point in the direction of the equator at the nearest hot pole (0° or 180°E). All scale bars are 10 km. (a) EN0230834860M, 28.2° S, 157.8°E, 129 m/pixel. The crater at the center of the image is ~6 km in diameter. (b) EN0223228194M, 31.8°S, 332.9°E, 73 m/pixel. The crater at the center of the image is ~12 km in diameter. (c) EN0223185654M, 40.1°S, 345.8°E, 98 m/pixel. The crater at the center of the image is ~23 km in diameter. (d) EN0226033266M, 59.7°N, 319.3°E, 24 m/pixel. The crater to the left of the arrow is ~4.5 km in diameter.

spectra and the laboratory analog spectra. The lack of an obvious absorption feature near a wavelength of 1000 nm (1 μm) has long suggested that Mercury's surface is dominated by silicates with low ferrous iron content [e.g., *Vilas*, 1988; *Blewett et al*., 1997, 2002; *Warell*, 2003; *Warell and Blewett*, 2004; *Warell et al*., 2006; *Robinson et al*., 2008; *Blewett et al*., 2009]. The two low-iron silicates in Figure 24, enstatite from the Peña Blanca Spring (PBS) aubrite [*Burbine et al*., 2002] and anorthite, have higher reflectances and higher 433 nm/749 nm ratios than the Mercury spectra.

[46] A dark, red component would be needed in a mixture with anorthite or PBS enstatite to move them down and to the left and so produce spectra like those of the Mercury surfaces. Troilite (iron sulfide, FeS) has appropriate characteristics, being relatively dark and red. However, the upper limit of ~4% Fe in Mercury's surface determined by the MESSENGER X-Ray Spectrometer [*Nittler et al*., 2011] places a strong constraint on the average amount of FeS that could be present at the surface. Ilmenite (Fe_2TiO_3) has a low reflectance and contributes to the low albedo of Ti-rich lunar mare basalts. However, like troilite, ilmenite is rich in iron and therefore cannot be a major component of Mercury's surface [*Denevi et al*., 2009; *Riner et al*., 2009, 2010]. Furthermore, X-Ray Spectrometer limits on titanium [~0.8 wt %, *Nittler et al*., 2011] are an even stronger constraint on average ilmenite abundance. Oldhamite (calcium sulfide, CaS) is found in meteorites with chemically reduced compositions [*Burbine et al*., 2002]. Oldhamite has the same color ratio as the Mercury spectra in Figure 24 but by itself is too bright and in addition has an absorption feature near 500 nm and a weaker band at ~950 nm. Other sulfides (MgS, MnS) also display absorptions in the wavelength range 500–600 nm [*Helbert et al*., 2012], although there is evidence that heating to Mercury daytime temperatures causes loss of the band and a decrease in spectral slope [*Helbert et al*., 2012]. The discovery of spectral changes that occur with heating indicates that caution is needed when interpreting spectra of candidate analog materials that were acquired at room temperature.

[47] Elemental sulfur, which could potentially be liberated in the hollows-forming process, is far brighter and far redder than the hollows. Although sulfur can exist in allotropes with different colors [e.g., *Nash*, 1987; *Greeley et al*., 1990; *Moses and Nash*, 1991], the boiling point of sulfur (~440°C at 1 atmosphere) is approximately equal to the highest Mercury daytime temperatures. Thus, it is unlikely that elemental sulfur could survive for long periods of time on the sunlit surface.

[48] Nano- or microphase opaque phases are capable of substantially lowering the reflectance of a mixture, and nanophase opaque minerals also cause reddening and diminution

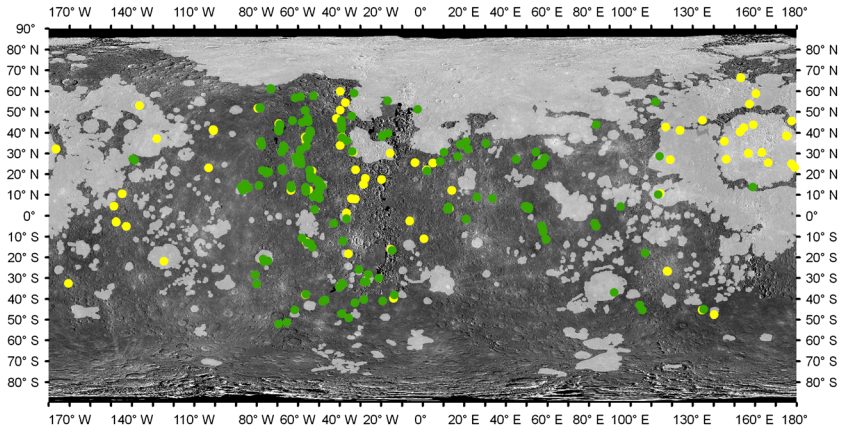

Figure 17. Locations of hollows on Mercury. Yellow dots show the locations of hollows mapped by *Blewett et al*. [2011]. Green dots are additional hollows identified from MESSENGER orbital images. The shaded light grey areas are smooth plains units mapped by *Denevi et al*. [2012]. Because of the spacecraft's highly eccentric orbit, images have better spatial resolution in the northern hemisphere, making identification of hollows easier there. The base image is a global MDIS monochrome mosaic in equirectangular projection.

of spectral absorption bands [e.g., *Hapke*, 2001; *Noble and Pieters*, 2003; *Noble et al*., 2007; *Lucey and Noble*, 2008; *Lucey and Riner*, 2011]. Thus, it is possible that finely disseminated sulfides (CaS, MgS, and/or FeS) occur in Mercury's LRM rocks, causing the characteristic low reflectance. When concentrated by impact melting [*Vaughan et al*., 2012] or assimilation of sulfur by Mg-rich magmas [*Helbert et al*., 2012], the sulfide phases could produce hollow-forming layers. Furthermore, given the observation that hollows are most closely associated with the LRM color unit, *Vaughan et al*. [2012] argued that LRM is sulfur-rich and thus that a sulfur-bearing compound is the darkening agent responsible for the low reflectance of the LRM.

[49] Mercury's degree of spectral variation is rather limited, as evidenced by the clustering of the de Graft spectra (diamonds) in Figure 24. The range of variation is less than that from an immature lunar highland soil to a mature one. *Lucey and Riner* [2011] and *Riner and Lucey* [2012] attributed Mercury's overall spectral character to the effects of a combination of nanophase and microphase metallic iron produced by space weathering on low-iron silicates, possibly with the presence of macroscopic opaque phases such as ilmenite or other opaque oxides [*Riner et al*., 2009, 2010]. The presence of opaque sulfides may thus cause the LRM to be darker than the other major Mercury color units (e.g., intermediate terrain and high-reflectance red plains

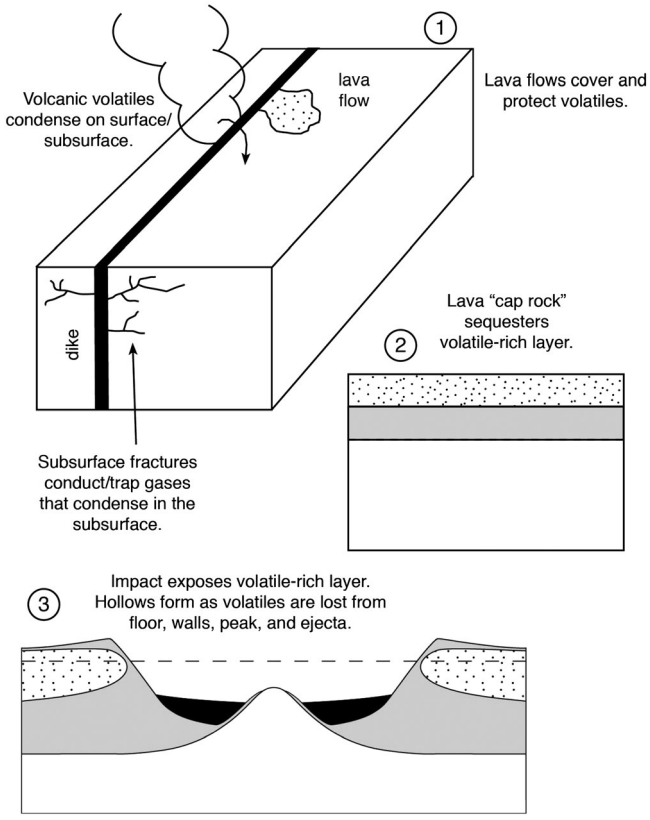

Figure 18. Schematic illustration of hollow formation by sequestration, impact exposure, and loss of magmatic volatiles.

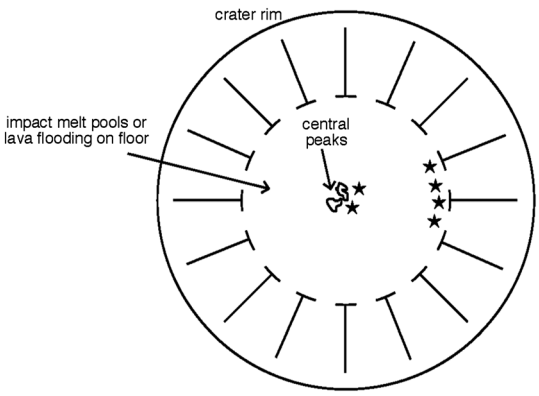

Figure 19. Schematic illustration of hollow formation by contact metamorphism. Heating of wall and peak material by shock, impact melt, volcanic flows, or intrusions could decompose volatile-bearing minerals, leading to the formation of hollows by mechanical failure of the remaining matrix. Hollows (stars) are initiated around topographic highs (walls and central peaks).

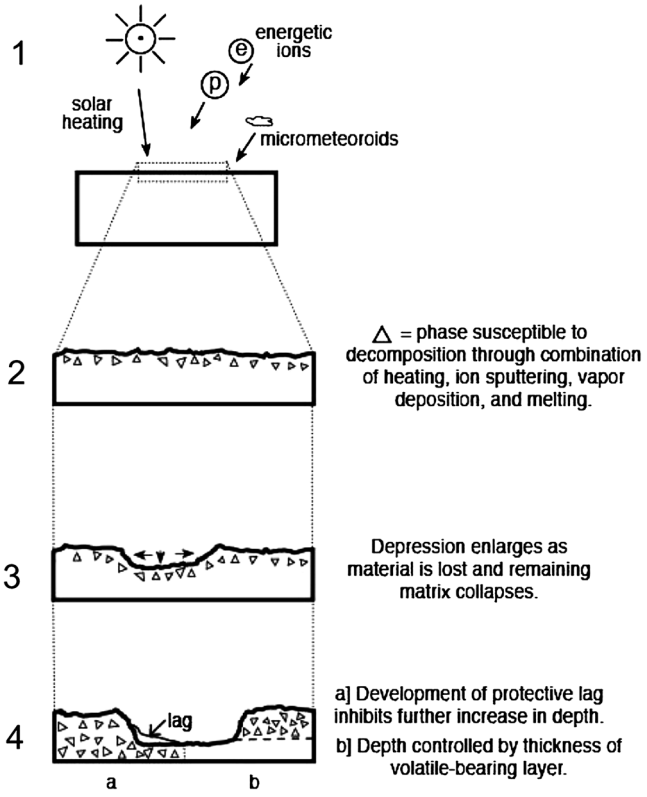

Figure 20. Schematic illustration of hollow formation by solar heating or space weathering. Some combination of high temperatures, ion sputtering, and micrometeoroid melting and vaporization decomposes volatile-bearing minerals, leading to formation of hollows by failure of the remaining matrix (sequence from 1 to 3). The depression stops increasing in depth when (4a) a protective armor of remnant material builds up, or (4b) the volatile-bearing layer has been consumed.

[*Robinson et al*., 2008; *Denevi et al*., 2009]). A key question then is: What causes the hollows to be (relatively) bright? Several mechanisms can be hypothesized, including:

[50] a. The presence of altered material. As mentioned in section 4, loss of "bulk" volcanic volatiles could expose alteration products generated during the time that the volatiles were buried.

[51] b. The presence of vapor-deposited coatings. Vaporized material generated in the hollow-forming process could "plate out" on the surroundings.

[52] c. The destruction of a darkening agent. Under the *Vaughan et al*. [2012] and *Helbert et al*. [2012] hypotheses, the sulfide darkening agent is concentrated and then lost because of exposure to the environment of the surface. This subtractive process could account for the high reflectance of active hollows. Sulfides (e.g., FeS and CaS, Figure 24) are red relative to iron-free silicates, so the loss of sulfides from a mineral assemblage would cause a decrease in spectral slope. Likewise, nanophase opaque minerals also cause reddening. Thus, the loss of nanophase sulfides would lead to a "bluer" mineral assemblage than one with nanophase sulfides still present.

[53] d. A physical difference such as smaller particle sizes or a special texture or scattering behavior. Whether the volatiles lost during hollow formation originated via the sequestration of condensed volcanic gases or were instead an inherent component of a crustal lithology, it is likely that the loss process would produce textures and particle-size distributions that differ from impact-generated regolith elsewhere on Mercury. Sublimation could loft small grains, producing deposits that have high reflectance due to small particle size and potentially high porosity (i.e., the "fairy castle" structure [*Hapke*, 2012] could be enhanced). The suggestion of fine-grained talus slopes at the base of hollows-bearing peak-ring mountains, e.g., in Raditladi (Figure 7), supports this hypothesis.

[54] In all cases, the high reflectance would be expected to fade with time as large and small impacts cause vertical and lateral mixing within Mercury's upper surface, and as the normal Mercury space weathering processes take over. This evolution could provide a sequential order for the observed range in the characteristics of hollows: those with bright interiors and halos would be most active, those with only bright interiors would be at a more advanced stage, and those for which interiors and exteriors match the background would be inactive.

6. Conclusions

[55] Mercury's hollows are unusual features that apparently have no counterpart in silicate material on other solar system bodies. In this contribution, we have cataloged the

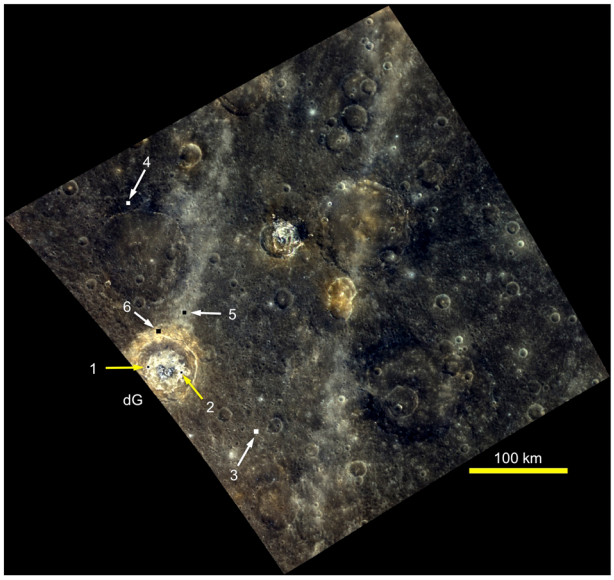

Figure 21. Color image of an area that includes crater de Graft (dG) and served as the case study for spectral reflectance; see also Figure 3. Areas for which spectra were extracted are marked by small black or white squares. 1 – hollows location 1. 2 – hollows location 2. 3 – intermediate terrain (IT). 4 – low-reflectance material (LRM). 5 – ray. 6 – red rim. Spectra are plotted in Figure 22 and represent 5×5, 9×9, or 11×11 pixel averages. The approximately parallel ray segments that cross the scene originated at Hokusai crater to the north. Color composite with 996, 749, and 433 nm wavelength as RGB (images EW0225143097I, EW0225143117G, and EW0225143101F, centered at 24.0°N, 6.7°E, 434 m/pixel).

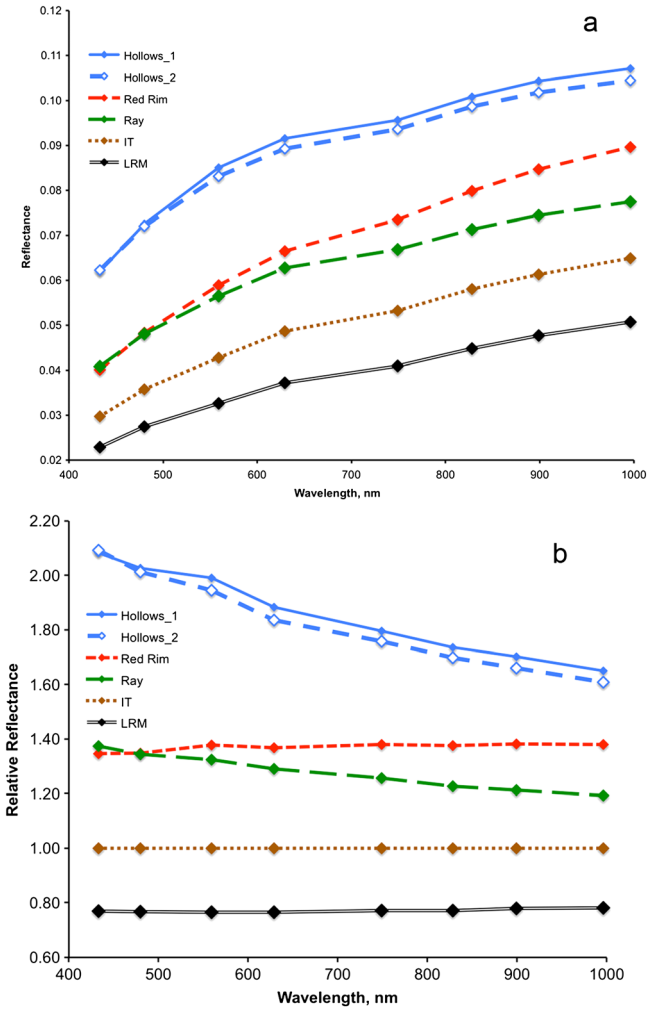

Figure 22. MDIS eight-color spectra for surfaces in and around de Graft crater. Locations from which the spectra were extracted are shown in Figure 21. (a) Reflectance spectra. Residual calibration errors or issues with the photometric normalization may cause the small dip in the spectra at 749 nm. (b) Spectra relative to the intermediate terrain (IT) emphasize differences in spectral slope.

variety of geological settings in which hollows occur. Global mapping of hollows shows that they occur in dark materials for which reflectance is lower than the planetary average (LRM or LBP). Hollows have not been found in high-reflectance smooth plains. Most hollows are found in or around impact structures, ranging from simple craters a few kilometers in diameter to multiring basins nearly two orders of magnitude larger. Morphological assessment indicates that the ages of the impact structures hosting hollows range from Kuiperian to Calorian. Hollows occur on crater and basin floors, walls, terraces, central peaks, and continuous ejecta. Some small clusters or isolated individual hollows are found in terrain not obviously related to impact structures, but these do appear to be found in locations of exposed dark material. At middle to high latitudes, hollows display some tendency to appear on slopes that face the equator or the nearest hot pole, implying that high temperatures figure in their formation process. As a potential morphological analog, the Moon's Ina-type features differ substantially in their characteristics from hollows.

[56] Hypotheses for the origin of hollows involve the loss of volatiles. The volatiles may have originated as volcanic exhalations that condensed onto the surface or in the subsurface and were buried by volcanic deposits, remaining in place until exposed by an impact. Under such a scenario, hollows could form by direct sublimation of the highly volatile phases. Alternatively, a volatile-bearing phase could exist as part of the host lithology. If this phase is destroyed when exposed at the surface (through some combination of low pressure, high temperatures, and intense micrometeoroid and energetic ion bombardment), hollows would form and grow as the phase is lost. The volatile-bearing phase could be present throughout the host rocks, it might be concentrated by impact melting and subsequent differentiation [*Vaughan et al.*, 2012], or the volatiles could have been assimilated by migrating melts [*Helbert et al.*, 2012].

[57] Our analysis of a multispectral image cube for the crater de Graft and surroundings demonstrates that Mercury surfaces are darker and redder than most candidate laboratory analogs. *Lucey and Riner* [2011] and *Riner and Lucey* [2012] attributed Mercury's low reflectance and red spectrum to the presence of nanophase and microphase metallic iron produced by intense space weathering. We suggest that finely disseminated sulfides (e.g., CaS, MgS, or FeS) could contribute to the low reflectance of the LRM relative to Mercury's average surface material [see also *Vaughan et al.* [2012] and *Helbert et al.* [2012]). The (relatively) high reflectance and characteristic blue color of hollows could be a consequence of the destruction of the darkening agent, of compositional differences related to altered minerals or vapor deposits, or of a physical state (grain size, texture,

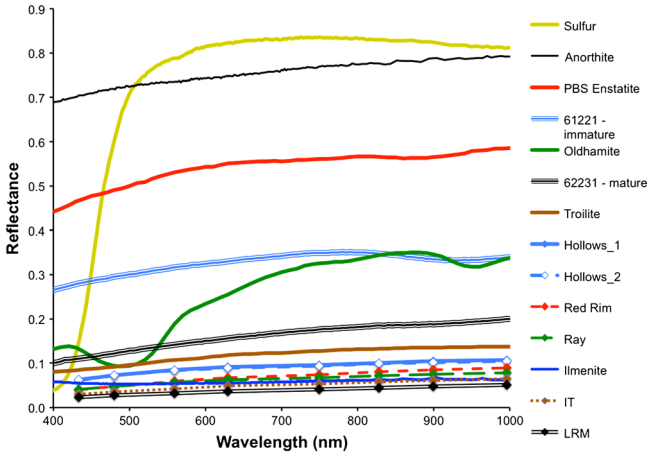

Figure 23. Laboratory reflectance spectra for analog minerals and two lunar soils, together with the Mercury spectra from Figure 22a. The following spectra are from RELAB: enstatite from Peña Blanca Spring (PBS) aubrite (TB-TJM-045/C1TB45), oldhamite (TB-TJM-038/C1TB38), troilite (TB-RPB-005/C1TB05), and lunar sample 61221 (LS-CMP-065-A/CALS65), and lunar sample 62231 (LS-CMP-030/CALS30). Spectra from the U.S. Geological Survey spectral library: sulfur (GDS 94 reagent), ilmenite (HS231.3B), and anorthite (GDS28 synthetic).

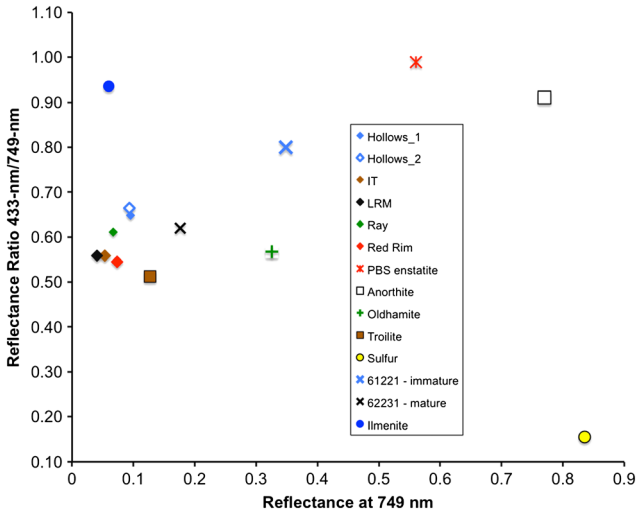

Figure 24. Ratio–reflectance plot for the spectra of Figure 23. The MDIS Mercury spectra are marked by diamonds. Greater values of the ratio correspond to shallower ("bluer") spectral slopes.

porosity, and/or scattering properties) that differs from that of impact-generated regolith elsewhere on the planet.

[58] Future work with radiative transfer mixing models is warranted to gain additional insights into the mineralogical composition of the variety of surfaces on Mercury, as well as the role of macroscopic, microphase, and nanophase opaque minerals in controlling Mercury's reflectance. More spectral studies of candidate analog materials heated to Mercury temperatures should be completed to better inform comparisons with observations of the planet. The photometric behavior of hollows and other surfaces, assessed by analysis of images obtained at widely varying illumination, viewing, and phase angles, can also provide clues to the particle size, porosity, and scattering characteristics of the terrain [*Domingue et al*., 2010].

[59] **Acknowledgments.** This work was made possible by financial support from a NASA MESSENGER Participating Scientist program grant (NNX08AN29G) to D.T.B., and by the MESSENGER project. The MESSENGER project is supported by the NASA Discovery Program under contracts NASW-00002 to the Carnegie Institution of Washington and NAS5-97271 to The Johns Hopkins University Applied Physics Laboratory (APL). We thank Mark Robinson for helpful comments and discussions. Anne Coté (Brown University) drafted Figures 18–20 and the geologic sketch maps. Brittany L. Young (University of Maryland, Baltimore County, and APL) assisted with figure and manuscript preparation. This research made use of spectra from the Brown University Reflectance Experiment Laboratory (RELAB).

References

Baker, D. M. H., J. W. Head III, S. C. Schon, C. M. Ernst, L. M. Prockter, S. L. Murchie, B. W. Denevi, S. C. Solomon, and R. G. Strom (2011), The transition from complex crater to peak-ring basin on Mercury: New observations from MESSENGER flyby data and constraints on basin formation models, *Planet. Space Sci.*, *15*, 1932–1948, doi:10.1016/j.pss.2011.05.010.

Blewett, D. T., P. G. Lucey, B. R. Hawke, G. G. Ling, and M. S. Robinson (1997), A comparison of mercurian reflectance and spectral quantities with those of the Moon, *Icarus*, *102*, 217–231.

Blewett, D. T., B. R. Hawke, and P. G. Lucey (2002), Lunar pure anorthosite as a spectral analog for Mercury, *Meteorit. Planet. Sci.*, *37*, 1245–1254.

Blewett, D. T., B. R. Hawke, P. G. Lucey, and M. S. Robinson (2007), A Mariner 10 color study of mercurian craters, *J. Geophys. Res.*, *112*, E02005, doi:10.1029/2006JE002713.

Blewett, D. T., M. S. Robinson, B. W. Denevi, J. J. Gillis-Davis, J. W. Head, S. C. Solomon, G. M. Holsclaw, and W. E. McClintock (2009), Multispectral images of Mercury from the first MESSENGER flyby: Analysis of global and regional color trends, *Earth Planet. Sci. Lett.*, *285*, 272–282, doi:10.1016/j.epsl.2009.02.021.

Blewett, D. T., B. W. Denevi, M. S. Robinson, C. M. Ernst, M. E. Purucker, and S. C. Solomon (2010), The apparent lack of lunar-like swirls on Mercury: Implications for the formation of lunar swirls and for the agent of space weathering, *Icarus*, *209*, 239–246, doi:10.1016/j.icarus.2010.03.008.

Blewett, D. T., et al. (2011), Hollows on Mercury: MESSENGER evidence for geologically recent volatile-related activity, *Science*, *333*, 1856–1859, doi:10.1126/science.1211681.

Boynton, W. V., A. L. Sprague, S. C. Solomon, R. D. Starr, L. G. Evans, W. C. Feldman, J. I. Trombka, and E. A. Rhodes (2007), MESSENGER and the chemistry of Mercury's surface, *Space Sci. Rev.*, *131*, 85–104.

Burbine, T. H., T. J. McCoy, L. R. Nittler, G. K. Benedix, A. Cloutis, and T. L. Dickinson (2002), Spectra of extremely reduced assemblages: Implications for Mercury, *Meteorit. Planet. Sci.*, *37*, 1233–1244.

Byrne, S., and A. P. Ingersoll (2003), A sublimation model for martian south polar ice features, *Science*, *299*, 1051–1053.

Cintala, M. J. (1992), Impact-induced thermal effects in the lunar and mercurian regoliths, *J. Geophys. Res.*, *97*, 947–973, doi:10.1029/91JE02207.

Denevi, B. W., and M. S. Robinson (2008), Mercury's albedo from Mariner 10: Implications for the presence of ferrous iron, *Icarus*, *197*, 239–246.

Denevi, B. W., et al. (2009), The evolution of Mercury's crust: A global perspective from MESSENGER, *Science*, *324*, 613–618, doi:10.1126/science.1172226.

Denevi, B. W., M. S. Robinson, S. L. Murchie, C. M. Ernst, P. K. Byrne, S. C. Solomon, and P. N. Peplowski (2012), The distribution of young plains on Mercury, *EPSC Abstracts and Program*, *7*, abstract EPSC2012-812.

Domingue, D. L., P. L. Koehn, R. M. Killen, A. L. Sprague, M. Sarantos, A. F. Cheng, E. T. Bradley, and W. E. McClintock (2007), Mercury's atmosphere: A surface-bounded exosphere, *Space Sci. Rev.*, *131*, 161–186, doi:10.1007/s11214-007-9260-9.

Domingue, D. L., et al. (2010), Whole-disk spectrophotometric properties of Mercury: Synthesis of MESSENGER and ground-based observations, *Icarus*, *209*, 101–124.

Domingue, D. L., S. L. Murchie, B. W. Denevi, N. L. Chabot, D. T. Blewett, N. R. Laslo, R. M. Vaughan, H. K. Kang, and M. K. Shepard (2011), Photometric correction of Mercury's global color mosaic, *Planet. Space Sci.*, *59*, 1873–1887, 2011.

Dzurisin, D. (1977), Mercurian bright patches: Evidence for physio-chemical alteration of surface material? *Geophys. Res. Lett.*, *4*, 383–386, doi:10.1029/GL004i010p00383.

El-Baz, F. (1973), "D-caldera": New photographs of a unique feature, in *Apollo 17 Preliminary Science Report*, pp. 30-13–30-17, NASA SP-330, U.S. Government Printing Office, Washington, D.C.

El Baz, F., and A. W. Worden, (1972), Visual observations from lunar orbit, in *Apollo 15 Preliminary Science Report*, pp. 25-1–25-25, NASA SP-289, U.S. Government Printing Office, Washington, D.C.

Ernst, C. M., S. L. Murchie, O. S. Barnouin, M. S. Robinson, B. W. Denevi, D. T. Blewett, J. W. Head, N. R. Izenberg, S. C. Solomon, and J. H. Roberts (2010), Exposure of spectrally distinct material by impact craters on Mercury: Implications for global stratigraphy, *Icarus*, *209*, 210–223, doi:10.1016/j.icarus.2010.05.022.

Evans, L. G., et al. (2012), Major-element abundances on the surface of Mercury: Results from the MESSENGER Gamma-Ray Spectrometer, *J. Geophys. Res.*, *117*, E00L07, doi:10.1029/2012JE004178.

Garry, W. B., M. S. Robinson, J. R. Zimbelman, J. E. Bleacher, B. R. Hawke, L. S. Crumpler, S. E. Braden, and H. Sato, (2012), The origin of Ina: Evidence for inflated lava flows on the Moon, *J. Geophys. Res.*, *117*, E00H31, doi:10.1029/2011JE003981.

Gillis-Davis, J. J., D. T. Blewett, R. W. Gaskell, B. W. Denevi, M. S. Robinson, R. G. Strom, S. C. Solomon, and A. L. Sprague (2009), Pit-floor craters on Mercury: Evidence for near-surface igneous activity, *Earth Planet. Sci. Lett.*, *285*, 243–250, doi:10.1016/j.bbr.2011.03.031.

Greeley, R., S. W. Lee, D. A. Crown, and N. Lancaster (1990), Observations of industrial sulfur flows: Implications for Io, *Icarus*, *84*, 374-402.

Hapke, B. (2001) Space weathering from Mercury to the asteroid belt, *J. Geophys. Res.*, *106*, 10,039–10,073.

Hapke, B. (2012), *Theory of Reflectance and Emittance Spectroscopy*, 2nd ed., Cambridge University Press, New York.

Hawkins, S. E., III, et al. (2007), The Mercury Dual Imaging System on the MESSENGER spacecraft, *Space Sci. Rev.*, *131*, 247–338.

Hawkins, S. E., III, et al. (2009), In-flight performance of MESSENGER's Mercury Dual Imaging System, in *Instruments and Methods for*

Astrobiology and Planetary Missions XII, edited by R. B. Hoover, G. V. Levin, A. Y. Rozanov, and K. D. Retherford, paper 74410Z, 12 pp., *SPIE Proceedings*, *7441*, SPIE, Bellingham, Wash.

Head, J. W., et al. (2008), Volcanism on Mercury: Evidence from the first MESSENGER flyby, *Science*, *321*, 69–72, doi:10.1126/science.1159256.

Head, J. W., et al. (2009), Volcanism on Mercury: Evidence From the first MESSENGER flyby for extrusive and explosive activity and the volcanic origin of plains, *Earth Planet Sci. Lett.*, *285*, 227–242, doi:10.1016/j.epsl.2009.03.007.

Head, J. W., et al. (2011), Flood volcanism in the northern high latitude of Mercury revealed by MESSENGER, *Science*, *333*, 1853–1856, doi:10.1126/science.1211997.

Helbert, J., A. Maturilli, M. D'Amore, W. M. Vaughan, J. W. Head, R. L. Klima, D. T. Blewett, and T. J. McCoy (2012), Spectral reflectance measurements of sulfides at the Planetary Emissivity Laboratory—Analogs for hollow-forming material on Mercury?, *Lunar Planet. Sci.*, *43*, abstract 1381.

Kerber, L., J. W. Head, S. C. Solomon, S. L. Murchie, D. T. Blewett, and L. Wilson (2009), Explosive volcanic eruptions on Mercury: Eruption conditions, magma volatile content, and implications for interior volatile abundances, *Earth Planet. Sci. Lett.*, *285*, 263–271, doi:10.1016/j.bbr.2011.03.031.

Kerber, L., J. W. Head, D. T. Blewett, S. C. Solomon, L. Wilson, S. Murchie, M. S. Robinson, B. W. Denevi, and D. L. Domingue (2011), The global distribution of pyroclastic deposits on Mercury: The view from MESSENGER flybys 1-3, *Planet. Space Sci.*, *59*, 1895–1909, doi:10.1016/j.bbr.2011.03.031.

Killen, R. M. (2003), Depletion of sulfur on the surface of the asteroid Eros and the Moon, *Meteorit. Planet. Sci.*, *38*, 383–388.

Kracher, A., and D. W. G. Sears (2005), Space weathering and the low sulfur abundance of Eros, *Icarus*, *174*, 36–45, doi:10.1016/j.icarus.2004.10.010.

Le Feuvre, M., and M. A. Wieczorek (2008), Nonuniform cratering of the terrestrial planets, *Icarus*, *197*, 291–306.

Le Feuvre, M., and M. A. Wieczorek (2011), Nonuniform cratering of the Moon and a revised crater chronology of the inner Solar System, *Icarus*, *214*, 1–20.

Loeffler, M. J., C. A. Dukes, W. Y. Chang, L. A. McFadden, R. A. Baragiola (2008), Laboratory simulations of sulfur depletion at Eros, *Icarus*, *195*, 622–629, doi:10.1016/j.icarus.2008.02.002.

Lucey, P. G., and S. K. Noble (2008), Experimental test of a radiative transfer model of the optical effects of space weathering, *Icarus*, *197*, 348–353.

Lucey, P. G., and M. A. Riner (2011), The optical effects of small iron particles that darken but do not redden: Evidence of intense space weathering on Mercury, *Icarus*, *212*, 451–462.

Malin, M. C., M. A. Caplinger, and S. D. Davis (2001), Observational evidence for an active surface reservoir of solid carbon dioxide on Mars, *Science*, *294*, 2146–2148, doi:10.1126/science.1066416.

Marchi, S., A. Morbidelli, and G. Cremonese (2005), Flux of meteoroid impacts on Mercury, *Astron. Astrophys.*, *431*, 1123–1127.

McClintock, W. E., et al. (2008), Spectroscopic observations of Mercury's surface reflectance during MESSENGER's first Mercury flyby, *Science*, *321*, 62–65, doi:10.1126/science.1159933.

McCord, T. B., and R. N. Clark (1979), The Mercury soil: Presence of Fe^{2+}, *J. Geophys. Res.*, *84*, 7664–7668.

Moses, J. I., and D. B. Nash (1991), Phase transformation and spectral reflectance of solid sulfur: Can metastable allotropes exist on Io?, *Icarus*, *89*, 277–304.

Murchie, S. L., et al. (2008), Geology of the Caloris basin, Mercury: A view from MESSENGER, *Science*, *321*, 73–76.

Nash, D. B. (1987), Sulfur in vacuum: Sublimation effects on frozen melts, and applications to Io's surface and torus, *Icarus*, *72*, 1–34.

Nittler L. R., L. G. Evans, R. D. Starr, J. Brückner, R. C. Reedy, W. V. Boynton, J. I. Trombka, J. O. Goldsten, J. Masarik, and T. J. McCoy (2001), Elemental composition from gamma-ray spectroscopy of the NEAR-Shoemaker landing site on 433 Eros, *Meteorit Planet Sci.*, *36*, 1639–1660.

Nittler, L. R., et al. (2011), The major-element composition of Mercury's surface from MESSENGER X-ray spectrometry, *Science*, *333*, 1847–1850, doi:10.1126/science.1211567.

Noble, S. K., and C. M. Pieters (2003), Space weathering on Mercury: Implications for remote sensing (in Russian), *Astron. Vestnik*, *37*, 34–39 (Engl. transl., *Sol. Syst. Res*., *37*, 31– 35.)

Noble, S. K., C. M. Pieters, and L. M. Keller (2007), An experimental approach to understanding the optical effects of space weathering, *Icarus*, *192*, 629–642.

Oberbeck, V. R., and R. H. Morrison (1973), On the formation of the lunar herringbone pattern, *Proc. Lunar Sci. Conf. 4th*, 107-123.

Peplowski, P. N., et al. (2011), Radioactive elements on Mercury's surface from MESSENGER: Implications for the planet's formation and evolution, *Science*, *333*, 1850–1852, doi:10.1126/science.1211576.

Peplowski, P. N., et al. (2012), Variations in the abundances of potassium and thorium on the surface of Mercury: Results from the MESSENGER Gamma-Ray Spectrometer, *J. Geophys. Res.*, *117*, E00L04, doi:10.1029/2012JE004141.

Potter, A. E. and T. H. Morgan (1985), Discovery of sodium in the atmosphere of Mercury, *Science*, *229*, 651–653, doi:10.1126/science.229.4714.651.

Potter, A. E. and T. H. Morgan (1986), Potassium in the atmosphere of Mercury, *Icarus*, *67*, 336–340.

Prockter, L. M., et al. (2010), Evidence for young volcanism on Mercury from the third MESSENGER flyby, *Science*, *329*, 668–671.

Rava, B., and B. Hapke (1987), An analysis of the Mariner 10 color ratio map of Mercury, *Icarus*, *71*, 397–429, doi:10.1016/j.bbr.2011.03.031.

Riner, M. A., and P. G. Lucey (2012), Spectral effects of space weathering on Mercury: The role of composition and environment, *Geophys. Res. Lett.*, *39*, L12201, doi:10.1029/2012GL052065.

Riner, M. A., P. G. Lucey, S. J. Desch, and F. M. McCubbin (2009), Nature of opaque components on Mercury: Insights into a mercurian magma ocean, *Geophys. Res. Lett.*, *36*, L02201, doi:10.1029/2008GL036128.

Riner, M. A., F. M. McCubbin, P. G. Lucey, G. J. Taylor, and J. J. Gillis-Davis (2010), Mercury surface composition: Integrating petrologic modeling and remote sensing data to place constraints on FeO abundance, *Icarus*, *209*, 301–313.

Robinson, M. S., and P. G. Lucey (1997), Recalibrated Mariner 10 color mosaics: Implications for mercurian volcanism, *Science*, *275*, 197–200.

Robinson, M. S., et al. (2008), Reflectance and color variations on Mercury: Regolith processes and compositional heterogeneity, *Science*, *321*, 66–69, doi:10.1126/science.1160080.

Robinson, M. S., P. C. Thomas, S. E. Braden, S. J. Lawrence, and W. B. Garry (2010), High resolution imaging of Ina: Morphology, relative ages, formation, *Lunar Planet. Sci.*, *41*, abstract 2592.

Sarantos, M., R. M. Killen, and D. Kim (2007), Predicting the long-term solar wind ion-sputtering source at Mercury, *Planet. Space Sci.*, *55*, 1584–1595.

Schon, S. C., J. W. Head, D. M. H. Baker, C. M. Ernst, L. M. Prockter, S. L. Murchie, and S. C. Solomon (2011), Eminescu impact structure: Insight into the transition from complex crater to peak-ring basin on Mercury, *Planet. Space Sci.*, *59*, 1949–1959, doi:10.1016/j.pss.2011.02.003.

Schultz, P. H. (1976), *Moon Morphology: Interpretations Based on Lunar Orbiter Photography*, 626 pp., Univ. of Texas Press, Austin, Tex.

Schultz, P. H. (1977), Endogenic modification of impact craters on Mercury, *Phys. Earth Planet. Inter.*, *15*, 202–912, doi:10.1016/j.bbr.2011.03.031.

Schultz, P. H., M. I. Staid, and C. M. Pieters (2006), Lunar activity from recent gas release, *Nature*, *444*, 184–186.

Slavin, J. A., et al. (2010), MESSENGER observations of extreme loading and unloading of Mercury's magnetic tail, *Science*, *329*, 665–668.

Spudis, P. D., and J. E. Guest (1988), Stratigraphy and geologic history of Mercury, in *Mercury*, edited by F. Vilas, C. Chapman, and M. S. Mathews, pp. 118–164, University of Arizona Press, Tucson, Ariz.

Staid, M., P. Isaacson, N. Petro, J. Boardman, C. M. Pieters, J. W. Head, J. Sunshine, K. Donaldson Hanna, and L. A. Taylor (2011), The spectral properties of Ina: New observations from the Moon Mineralogy Mapper, *Lunar Planet Sci.*, *42*, abstract 2499.

Stockstill-Cahill, K. R., T. J. McCoy, L. R. Nittler, S. Z. Weider, and S. A. Hauck II (2012), Magnesium-rich crustal compositions on Mercury: Implications for magmatism from petrologic modeling, *J. Geophys. Res.*, *117*, E00L15, doi:10.1029/2012JE004140.

Stooke, P. J. (2012), Lunar meniscus hollows, *Lunar Planet. Sci.*, *43*, abstract 1011.

Strain, P., and F. El Baz (1980), The geology and morphology of Ina, *Proc. Lunar Planet. Sci. Conf. 11th*, 2437–2446.

Strom, R. G., C. R. Chapman, W. J. Merline, S. C. Solomon, and J. W. Head (2008), Mercury cratering record viewed from MESSENGER's first flyby, *Science*, *321*, 79–81.

Trombka, J. I., et al. (2000), The elemental composition of asteroid 433 Eros: Results of the NEAR-Shoemaker X-ray spectrometer, *Science*, *289*, 2101-2105, doi:10.1126/science.289.5487.2101.

Vaughan, W. M., J. Helbert, D. T. Blewett, J. W. Head, S. L. Murchie, K. Gwinner, T. J. McCoy, and S. C. Solomon (2012), Hollow-forming layers in impact craters on Mercury: Massive sulfide deposits formed by impact melt differentiation?, *Lunar Planet Sci.*, *43*, abstract 1187.

Vilas, F. (1988), Surface composition of Mercury from reflectance spectrophotometry, in *Mercury*, edited by F. Vilas, C. R. Chapman, and M. S. Matthews, pp. 59–76, University of Arizona Press, Tucson, Ariz.

Warell, J. (2003), Properties of the hermean regolith III: Disk resolved vis-NIR reflectance spectra and implications for the abundance of iron, *Icarus 161*, 1992–222.

Warell, J., and D. T. Blewett (2004), Properties of the hermean regolith V: New optical reflectance spectra, comparison with lunar anorthosites, and mineralogical modeling, *Icarus*, *168*, 257–276.

Warell, J., A. L. Sprague, J. P. Emery, R. W. H. Kozlowski, and A. Long (2006), The 0.7-5.3 μm IR spectra of Mercury and the Moon: Evidence for high-Ca clinopyroxene on Mercury, *Icarus*, *180*, 281–291.

Warell, J., A. Sprague, R. Kozlowski, D. A. Rothery, N. Lewis, J. Helbert, and E. Cloutis (2010), Constraints on Mercury's surface composition from MESSENGER and ground-based spectroscopy, *Icarus*, *209*, 138–163.

Weider, S. Z., L. Nittler, R. D. Starr, T. McCoy, K. Stockstill-Cahill, P. K. Byrne, B. W. Denevi, J. W. Head, and S. C. Solomon (2012), Chemical heterogeneity on Mercury's surface revealed by the MESSENGER X-Ray Spectrometer, *J. Geophys. Res.*, *117*, E00L05, doi:10.1029/2012JE004153.

Whitaker, E. A. (1972), An unusual mare feature, in *Apollo 15 Preliminary Science Report*, pp. 25-84–25-85, NASA SP 289, U.S. Government Printing Office, Washington, D.C.

Xiao, Z., and R. G. Strom (2012), Problems determining relative and absolute ages using the small crater population, *Icarus*, *220*, 254–267.

Xiao, Z., et al. (2012), The youngest geologic terrains on Mercury, *Lunar Planet Sci.*, *43*, abstract 2143.